MESO-SCALE METHOD OF ASYMPTOTIC ANALYSIS OF ELASTIC VIBRATIONS IN PERIODIC AND NON-PERIODIC MULTI-STRUCTURES

by M. J. NIEVES[†]

(*School of Computer Science and Mathematics, Keele University, Keele ST5 5BG, UK*)

A. B. MOVCHAN

(*Department of Mathematical Sciences, University of Liverpool, Liverpool L69 7ZL, UK*)

Summary

The method of meso-scale asymptotic approximations has proved to be very effective for the analysis of models of solids containing large clusters of defects, such as small inclusions or voids. Here, we present a new avenue where the method is extended to elastic multi-structures. Geometrically, a multi-structure makes a step up in the context of overall dimensions, compared to the dimensions of its individual constituents. The main mathematical challenge comes from the analysis of the junction regions assigned to the multi-structure itself. Attention is given to problems of vibration and on the coupling of vibration modes corresponding to displacements of different orientations. The method is demonstrated through the dynamic analysis of infinite or finite multi-scale asymmetric flexural systems consisting of a heavy beam connected to a non-periodic array of massless flexural resonators within some interval. In modelling the interaction between the beam and the resonators, we derive a vectorial system of partial differential equations through which the axial and flexural motions of the heavy beam are coupled. The solution of these equations is written explicitly in terms of Green's functions having intensities determined from a linear algebraic system. The influence of the resonators on the heavy beam is investigated within the framework of scattering and eigenvalue problems. For large collections of resonators, dynamic homogenization approximations for the medium within the location of the resonant array are derived, leading to (i) the classical Rayleigh beam for symmetric systems and (ii) a generalized Rayleigh beam for asymmetric structures that support flexural–longitudinal wave coupling. Independent numerical simulations are also presented that demonstrate the accuracy of the analytical results.

1. Introduction

The method of meso-scale asymptotic approximations (**1**, **2**) provides an effective breakthrough for problems normally considered as non-treatable by analytical means that gives a pointwise description of the fields around defects within a cluster. Typically, if one has to deal with modelling a large cluster of inclusions or impurities of different types embedded in an elastic solid, the popular approach would be to resort to the methods involving the analysis of random media and homogenisation, which exclude information about the immediate neighbourhood of inclusions. On the other hand, in many instances the use of modern technologies would provide essential data through scans with

[†]Corresponding author <m.nieves@keele.ac.uk>

coordinates of inclusions within the cluster, as well as their typical size and shape. Indeed, the pointwise description of the physical fields around the inclusions is also important in the context of the evaluation of the stress concentration and identification of the dynamic defect modes. The work (1, 2), in turn, is based on the fundamental studies (3, 4) of singularly perturbed problems based on the method of compound asymptotic expansions, which opens up larger avenues in the context of higher order approximations, compared to popular approaches based on matched asymptotics.

In the book (2) and the papers (1, 5–10), the method of meso-scale asymptotic approximations has been applied both to the scalar problems, related to Laplace's operator, as well as vector problems of linear elasticity and electromagnetism. Furthermore, the method has been extended in (11) to problems of elastic vibrations for solids containing structured inertial interfaces.

In the present article, we address the question of modelling meso-scale clusters for elastic multi-structures. We choose to study flexural multi-structures, where a main beam is connected to a large cluster of beams, and the emphasis is made on their combined dynamic response, rather than a solution of a static boundary value problem.

Models of flexural multi-scale systems have great importance in civil engineering and can represent a multitude of structures including bridges, bridge decks, buildings, pipeline systems, rooftops, etc. Hence, understanding their dynamic behaviour is paramount in mitigating catastrophic risks to society. Engineering structures such as the aforementioned often possess elongated and slender members relative to their overall size. Additionally, they generally have periodic assemblies, paving the way to highly accurate lower-dimensional models that describe the behaviour of these structures and their failure with the use of fundamental mechanical elements including beams, rods, masses, dampers etc. In connection with improving safety of engineering systems through similar modelling approaches, we briefly highlight the study of damage evolution (12, 13) within and dynamic failure (14–17) of flexural systems owing to external loading that also plays a crucial role in this paradigm.

Flexural stratified systems have wide application in the design of structured waveguides and vice versa. In fact, in comparison with numerical and experimental approaches, analytical models describing these waveguides are key to the cost-effective design of a novel range of materials whose microstructure helps them to undergo extraordinary and counter-intuitive responses. The flexural media we consider here, use an internal resonant microstructure to bestow the master structure with negative inertial effects for translation and rotation. In connection with the latter, the rotational inertia has played a key role in creating anisotropic dynamic responses in networks of Rayleigh beams (18–21). Further, collections of resonators have paved the way for innovative 'meta-surfaces' for elastic layers (22, 23) to convert surface waves to bulk waves.

Examples of lattice-type models related to the present work include one-dimensional (1D) models for stratified passive flexural systems (21, 24, 25), elastic periodic materials with self-similar dispersive properties owing to their microstructure (26), graded resonant waveguides for enhancing wave attenuation (27) and 1D waveguides that support edge modes (28). In contrast to linear wave theory, we mention that nonlinear dynamic phenomena concerning flexural–longitudinal wave coupling has also been studied in 1D elastic systems under configurational forces in (29). Further, flexible materials that utilise large deformations to manipulate waves of finite amplitudes have also been constructed (30, 31).

Further, periodically placed active gyroscopic components have been used to couple dynamic elastic responses in beams (32, 33) and 1D elastic (34) and flexural (35) waveguides, where the latter at low-frequency approximate Rayleigh gyrobeams (33). One may also employ gyroscopes to

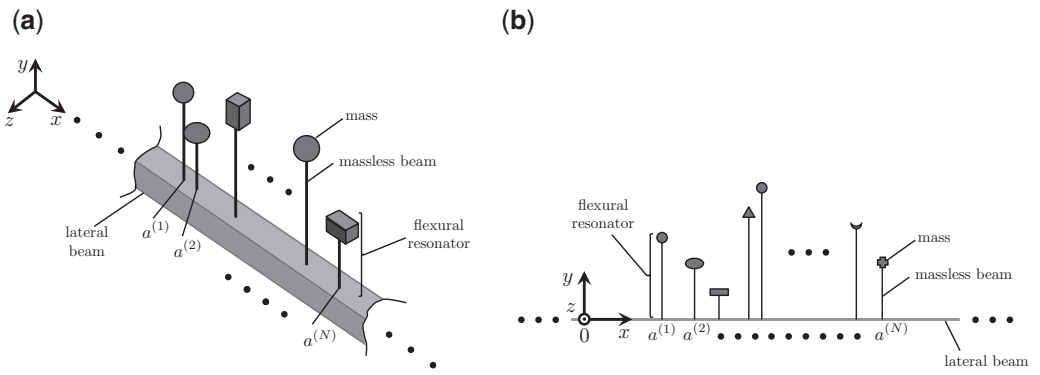

Fig. 1 Examples of an infinite beam axially aligned with the x-axis and attached to N flexural resonators aligned parallel to the positive y-axis. (a) A 3D schematic of the system and (b) the two-dimensional view of such a system in the xy-plane, where we address the motion of this system.

provide a dynamic coupling between flexural and longitudinal motions of a beam, but in contrast, here, we develop a model of a passive system that reproduces this phenomenon.

The multi-coupling of wave phenomena in passive media is an crucial paradigm in engineering design, for instance of structures with important applications in piping, power and process industries (**36**). Further, similar coupling effects are being exploited in the design of innovative soft-robotic devices (**37**, **38**). Multi-coupling of waves has been investigated in the framework of periodic elastic systems in the last 50 years. Theoretical advances in approaches for analysing this phenomenon were developed by Mead (**39**). The interaction between flexural and longitudinal waves in damped plates with periodic stiffeners has been analysed in (**40**). Flexural–longitudinal coupling of waves in infinite periodic flexural structures with transverse arrays of beams has been considered in (**41**), where it is shown that the transverse members can enhance wave transmission within the medium. This coupling has also been numerically and experimentally studied in the context of a frequency response analysis for the forcing of finite periodic flexural systems (**42**). Analytical and experimental studies of the multi-coupling of waves in forced systems has appeared in (**43**, **44**). A unified theoretical approach for determining the response of general classes of elastic systems with discrete or continuous microstructures has been recently developed in (**45**).

In contrast to those problems mentioned above, here we focus on modelling the dynamic behaviour of a class of flexural systems that have a non-periodic microstructure. Namely, we consider a beam attached to a non-periodic arrangement of massless flexural resonators, as shown in Fig. 1, that within certain frequency regimes contribute negative translational or rotational inertial effects to the remaining structure. We refer to this structure as a comb multi-structure or comb in this article. The considered scenario removes the opportunity of using the techniques that use Fourier transforms, Floquet–Bloch conditions etc.; all requiring a geometrical periodicity for their application.

On the other hand, we develop analytical tools aimed at recovering the behaviour of such systems, which includes capturing effects associated with dynamic interactions within the microstructure at any given frequency.

The application of resonators in controlling wave phenomena in solids also provides new avenues for the design of structured materials. Several types of resonators that adjust the translational inertial

properties of the remaining medium have been considered in (**46**) for infinite systems of spring-like points, (**47**, **48**) where the influence of various infinite mass-spring arrays on flexural wave propagation is considered and (**49**), which contains the analysis of localisation around structured resonant rings of point masses and mass-spring resonators. With respect to the analytical modelling of vibration in finite systems with non-periodic collections of point defects, see (**50**), where eigenfrequencies and eigenfunctions for thick plates possessing sparsely distributed point masses have been determined.

Recently, numerical models have been employed to investigate the role of non-periodic arrays of compressional resonators in converting elastic surface waves into bulk waves in a two-dimensional elastic medium. This approach has led to the design of innovative seismic protection systems (**22**) inspired by interactions between earthquakes and forests (**23**). Effective models governing surface wave propagation of analogous periodic systems involving flexural periodic systems have been derived in (**51**). Effective boundary conditions for three-dimensional elastic bodies with arrays of flexural resonators have been studied in (**52**, **53**), where the scattering of bulk waves by metasurfaces has also been considered.

In relation to these studies, we mention the analytical tools we develop and employ in this article are highly accurate in a range of meso-scale scenarios. They are applicable to beams with sparse non-regular arrangements of resonators, dense non-periodic clusters of resonators and, as demonstrated here, they also naturally lead to dynamic homogenisation approximations for periodic configurations. In the latter configuration, one may also extract essential information about effective wavenumbers (both real and complex) that govern the propagation of wave and evanescent modes inside densely packed periodic medium. In connection with analysing effective wavefields for complex and random media, we mention the investigations carried out in (**54**–**57**).

In section 2, we derive the equations governing the behaviour of the infinite asymmetric flexural medium shown in Fig. 1, which contains an interval that is attached to a non-periodic array of flexural resonators. Section 3 is dedicated to the derivation of the solution of this model with the use of Green's functions. In section 4, we concentrate on the case of a single resonator attached to the beam and demonstrate the dynamic influence this resonator has on waveforms propagating through the beam in the context of a scattering problem. In section 5, we show how the theory of sections 2 and 3 can be used within the framework of a dynamic homogenisation to obtain a model describing a generalised Rayleigh beam, for systems with a large periodic cluster of resonators. We also derive the effective boundary conditions for this effective medium in Appendix A, which is used to consider the scattering of flexural waves by a periodic cluster of resonators in section 5. Section 6 contains the treatment of eigenvalue problems for finite flexural systems with non-periodic clusters of flexural resonators, where we also present a procedure to compute the entire spectrum of such systems and the corresponding modes. Section 7 is devoted to derivation of dynamic homogenisation approximations, based on meso-scale solutions, for Rayleigh beams that can possess negative translational and rotational inertia, where further details of these derivations can be found in Appendix B. Finally, in section 8, we end with some conclusions and discussion concerning the present work.

2. Formulation of the meso-scale problem: model problems

We consider the comb multi-structure as shown in Fig. 1, which is composed of an infinite beam aligned axially with the x-axis and possessing a density ρ, cross-sectional area A, Young's modulus E and second moment of area J. Attached to this lateral beam are N flexural resonators directed parallel with the y-axis and whose bases are positioned at $a^{(j)}$ along the infinite beam. The jth resonator is

formed from massless flexural beams of length L_j, Young's modulus E_j, cross-sectional area A_j and second moment of area J_j, $1 \le j \le N$. The tip of the jth massless beam is connected to a node of mass m_j and moment of inertia I_j^z, $1 \le j \le N$, around the z-axis. For simplicity, we consider the flexural and axial motions of members forming this system taking place only in the xy-plane.

2.1 *The model problem for the main elastic beam*

In the considered problem, the equations governing the motion of the resonators can be dispensed by capturing the effective contributions of these elements in deriving a system of coupled differential equations that dictate the behaviour of the lateral beam. Namely, we consider the time-harmonic motion of the system and look for the displacement amplitudes $U(x)$ and $V(x)$, representing axial and transverse motions of the lateral infinite beam. These displacement functions satisfy

$$\rho A\omega^2 U(x) + EAU''(x) = -\sum_{1\le j\le N} \omega^2 \left[\Psi_j(\omega)U(a^{(j)}) + \Pi_j(\omega)V'(a^{(j)})\right]\delta(x-a^{(j)}), \tag{1}$$

and

$$\begin{aligned} -\rho A\omega^2 V(x) + EJV''''(x) = &\sum_{1\le j\le N} \omega^2 \Phi_j(\omega)V(a^{(j)})\delta(x-a^{(j)}) \\ &- \sum_{1\le j\le N} \omega^2 \left[\Pi_j(\omega)U(a^{(j)}) + \Upsilon_j(\omega)V'(a^{(j)})\right]\delta'(x-a^{(j)}), \end{aligned} \tag{2}$$

for $-\infty < x < \infty$. Here, the coefficients of the Dirac delta functions and its derivatives in the above right-hand sides are rational functions of the radian frequency ω of vibration, given as

$$\Phi_j(\omega) = \frac{E_jA_jm_j}{E_jA_j - m_j\omega^2L_j},$$

$$\Pi_j(\omega) = \frac{6E_jJ_jL_jm_j(L_jI_j^z\omega^2 - 2E_jJ_j)}{\mathcal{D}_j}, \qquad \Psi_j(\omega) = -\frac{12E_jJ_jm_j(L_jI_j^z\omega^2 - E_jJ_j)}{\mathcal{D}_j}$$

$$\text{and} \qquad \Upsilon_j(\omega) = -\frac{4E_jJ_j(-3[L_j^2m_j + I_j^z]E_jJ_j + I_j^zL_j^3m_j\omega^2)}{\mathcal{D}_j}, \tag{3}$$

with

$$\mathcal{D}_j = I_j^zL_j^4m_j\omega^4 - 4L_jE_jJ_j(L_j^2m_j + 3I_j^z)\omega^2 + 12E_j^2J_j^2.$$

2.2 *Illustrative derivation of the governing equations for the displacement field in the main beam*

In what follows, we now derive the form of the coupled differential equations (1) and (2) governing the motion of the lateral beam. We begin by writing the linear momentum balance for the lateral beam in the form

$$\rho A\omega^2 U(x) + EAU''(x) = -\sum_{1\le j\le N} \mathcal{Q}^{(x,j)}\delta(x-a^{(j)}), \tag{4}$$

$$-\rho A\omega^2 V(x) + EJV''''(x) = \sum_{1\le j\le N}\left[\mathcal{F}^{(y,j)}\delta(x-a^{(j)}) - \mathcal{M}^{(z,j)}\frac{d}{dx}\delta(x-a^{(j)})\right], \tag{5}$$

where $-\infty < x < \infty$ and the action of the resonators on the lateral beam has been modelled as point forces and moments represented by the appearance of the Dirac delta function δ and its derivatives, respectively. The intensities of these quantities are determined by the axial force $F^{(y,j)}$ parallel to the y-direction, the shear force $\mathcal{Q}^{(x,j)}$ exerted in the x-direction and the moment $\mathcal{M}^{(z,j)}$ applied around the z-axis by the jth resonator. In the next section, we derive the form of these quantities.

2.3 *Model problems for individual resonators*

In order to derive the forcing and turning force intensities found in (4) and (5) due to the resonators, one needs to consider the axial and flexural motions of these elements. We begin by deriving the resonators' effective contribution to the lateral beam owing to their axial motion, before moving to the study of the contribution of the flexural motion of the resonators in section 2.3.2.

2.3.1 Axial motion of a resonator. The axial motion of the jth resonator is determined by the function $V^{(j)}(\hat{y})$, that satisfies:

$$(V^{(j)})''(\hat{y}) = 0$$

for $0 \le \hat{y} \le L_j$, where $\hat{y}$ is the local coordinate of the resonator. This function is also subject to the conditions:

$$V^{(j)}(0) = V(a^{(j)}), \quad V^{(j)}(L_j) = v_j.$$

Here, v_j is the longitudinal displacement amplitude of the mass at the resonator's tip. The displacement function is therefore given by

$$V^{(j)}(\hat{y}) = (v_j - V(a^{(j)}))\frac{\hat{y}}{L_j} + V(a^{(j)}). \tag{6}$$

The linear momentum balance for the mass at the tip then yields the equation

$$-m_j\omega^2 v_j = -F^{(y,j)}(L_j), \tag{7}$$

with

$$F^{(y,j)}(\hat{y}) = E_jA_j(V^{(j)})'(\hat{y})$$

being the internal axial force experienced by the resonator. It follows from (7) and (6) that the term $\mathcal{F}^{(y,j)}$ in (5) can be written completely in terms of the lateral beam's displacement at the base of the resonator as follows:

$$\mathcal{F}^{(y,j)} = F^{(y,j)}(0) = \omega^2\Phi_j(\omega)V(a^{(j)}), \tag{8}$$

where $\Phi_j(\omega)$ is given in (3).

2.3.2 Flexural motion of a resonator. Flexure of the jth resonator in the x-direction is governed by

$$(U^{(j)})''''(\hat{y}) = 0, \qquad \text{for} \qquad 0 \le \hat{y} \le L_j,$$

where $U^{(j)}$ is the flexural displacement amplitude, acting parallel to the x-axis, for the massless beam. Here, $U^{(j)}$ may be determined using the preceding equation and the boundary conditions involving the displacements and rotations

$$\Theta^{(z,j)}(\hat{y}) = -(U^{(j)})'(\hat{y})$$

about the z-axis at the end of the beam:

$$U^{(j)}(0) = U(a^{(j)}), \qquad U^{(j)}(L_j) = u_j,$$

$$\Theta^{(z,j)}(0) = \Theta^z(a^{(j)}), \qquad \Theta^{(z,j)}(L_j) = \theta_j^z.$$

Here, u_j and θ_j^z are generalised coordinates of the mass at the tip of the beam representing the amplitudes of its displacement in the x-direction and rotation about the z-axis, respectively, and

$$\Theta^z(a^{(j)}) = V'(a^{(j)}),$$

is the amplitude of rotation of the lateral beam about the z-axis at the jth junction. The function $U^{(j)}$ is then found to be:

$$\begin{aligned} U^{(j)}(\hat{y}) = &-[(\theta_j^z + \Theta(a^{(j)}))L_j + 2(u_j - U(a^{(j)})]\frac{\hat{y}^3}{L_j^3} \\ &+[3(u_j - U(a^{(j)})) + L_j(\theta_j^z + 2\Theta^z(a^{(j)})]\frac{\hat{y}^2}{L_j^2} \\ &-\Theta^z(a^{(j)})\hat{y} + U(a^{(j)}). \end{aligned} \tag{9}$$

2.3.3 Identifying the shear force and moment applied at the junctions. To determine $\mathcal{Q}^{(x,j)}$ and $\mathcal{M}^{(z,j)}$ in (4) and (5), we require the linear and angular momentum balance of the mass at the tip of the resonator. The linear momentum principle in the x-direction is

$$-m_j\omega^2 u_j = -Q^{(x,j)}(L_j), \tag{10}$$

whereas the angular momentum balance about the z-axis takes the form

$$-I_z^{(j)}\omega^2\theta_j^z = -M^{(z,j)}(L_j), \tag{11}$$

where the internal shear forces and moments are:

$$Q^{(x,j)}(\hat{y}) = -E_jJ_j(U^{(j)})'''(\hat{y}), \quad \text{and} \quad M^{(z,j)}(\hat{y}) = -E_jJ_j(U^{(j)})''(\hat{y}),$$

respectively. Upon substitution of (9) into (10) and (11), one can obtain

$$\begin{aligned} \mathcal{Q}^{(x,j)} &= Q^{(x,j)}(0) = \omega^2\Psi_j(\omega)U(a^{(j)}) + \omega^2\Pi_j(\omega)V'(a^{(j)}), \\ \mathcal{M}^{(z,j)} &= M^{(z,j)}(0) = \omega^2\Pi_j(\omega)U(a^{(j)}) + \omega^2\Upsilon_j(\omega)V'(a^{(j)}), \end{aligned} \tag{12}$$

where the rational functions Ψ_j, Π_j and Υ_j of the radian frequency ω are found in (3).

2.4 *The comb multi-structure*

Thus using (4), (5), (8) and (12) we have the axial and flexural displacement of the lateral beam, $U(x)$ and $V(x)$, respectively, satisfy

$$\rho A\omega^2 U(x) + EAU''(x) = -\sum_{1\le j\le N} \omega^2 \left[\Psi_j(\omega)U(a^{(j)}) + \Pi_j(\omega)V'(a^{(j)})\right]\delta(x-a^{(j)}),$$

and

$$-\rho A\omega^2 V(x) + EJV''''(x) = \sum_{1\le j\le N} \omega^2 \Phi_j(\omega)V(a^{(j)})\delta(x-a^{(j)}) - \sum_{1\le j\le N} \omega^2 \left[\Pi_j(\omega)U(a^{(j)}) + \Upsilon_j(\omega)V'(a^{(j)})\right]\delta'(x-a^{(j)}),$$

for $-\infty < x < \infty$, where Φ_j, Ψ_j, Π_j and Υ_j are given in (3). Here it is clearly seen from the above right-hand sides that the action of the resonators couples the axial and flexural motions of the beam. Further, we comment that the coupling effect may be eliminated by either considering a comb multi-structure that is symmetric about the x-axis or by considering special frequency regimes where certain rational functions in the above right-hand side become zero. These facts are further investigated in section 7, but for now, we focus on the solution to the above equations and the effect of the coupling on vibrations propagating in the considered system.

3. The displacement field in the meso-scale multi-structure

The solution of (1) and (2) can be traced by using the Green's functions g and G defined as solutions of

$$\rho A\omega^2 g(x) + EAg''(x) + \delta(x) = 0, \tag{13}$$

$$-\rho A\omega^2 G(x) + EJG''''(x) + \delta(x) = 0, \tag{14}$$

with $-\infty < x < \infty$. According to the above, the functions g and G represent the response of the lateral beam to an oscillating point force at the origin in the x- and y-directions, respectively. They are also bounded and take the complex representations:

$$g(x) = \frac{i}{2EAk_R}\exp\left(ik_R|x|\right),$$

$$G(x) = \frac{1}{4EJk_B^3}\Big[\exp(-k_B|x|) - i\exp(ik_B|x|)\Big],$$

with

$$k_R = \left(\frac{\rho\omega^2}{E}\right)^{1/2}, \qquad k_B = \left(\frac{\rho A\omega^2}{EJ}\right)^{1/4}$$

being the wavenumbers for the axial and flexural vibration of the beam, respectively. The solutions $U(x)$ and $V(x)$ of (1) and (2) then take the form:

$$\begin{aligned} U(x) &= \sum_{1\le j\le N} \omega^2 \left[\Psi_j(\omega)U(a^{(j)}) + \Pi_j(\omega)V'(a^{(j)})\right] g(x-a^{(j)}), \\ V(x) &= -\sum_{1\le j\le N} \omega^2 \Phi_j(\omega)V(a^{(j)})G(x-a^{(j)}) \\ &\quad + \sum_{1\le j\le N} \omega^2 \left[\Pi_j(\omega)U(a^{(j)}) + \Upsilon_j(\omega)V'(a^{(j)})\right] G'(x-a^{(j)}). \end{aligned} \tag{15}$$

The unknown coefficients $U(a^{(j)})$, $V(a^{(j)})$ and $V'(a^{(j)})$ in the above right-hand sides can be obtained through an algebraic system arriving from the computation of these quantities with (15).

3.1 *Derivation of the algebraic system*

We compute the left-hand sides of (15) at $x = a^{(j)}$ and also compute the derivative of V in (15) at these points. In doing so, we obtain

$$U(a^{(k)}) = \sum_{1\le j\le N} \omega^2 \left[\Psi_j(\omega)U(a^{(j)}) + \Pi_j(\omega)V'(a^{(j)})\right] g(a^{(k)}-a^{(j)}) \tag{16}$$

$$\begin{aligned} V(a^{(k)}) &= -\sum_{1\le j\le N} \omega^2 \Phi_j(\omega)V(a^{(j)})G(a^{(k)}-a^{(j)}) \\ &\quad + \sum_{1\le j\le N} \omega^2 \left[\Pi_j(\omega)U(a^{(j)}) + \Upsilon_j(\omega)V'(a^{(j)})\right] G'(a^{(k)}-a^{(j)}) \end{aligned} \tag{17}$$

and

$$\begin{aligned} \frac{dV}{dx}(a^{(k)}) &= -\sum_{1\le j\le N} \omega^2 \Phi_j(\omega)V(a^{(j)})G'(a^{(k)}-a^{(j)}) \\ &\quad + \sum_{1\le j\le N} \omega^2 \left[\Pi_j(\omega)U(a^{(j)}) + \Upsilon_j(\omega)V'(a^{(j)})\right] G''(a^{(k)}-a^{(j)}). \end{aligned} \tag{18}$$

Before moving to the determination of $U(a^{(j)})$, $V(a^{(j)})$ and $V'(a^{(j)})$, next we look at a simplified representation of the above system.

3.2 *Alternative representation of the algebraic system*

The homogeneous system (16)–(18) can be written in a more compact form as follows:

$$(\boldsymbol{I}_{3N} + \omega^2 \boldsymbol{D}_N(\omega))\boldsymbol{U} = \boldsymbol{0}, \tag{19}$$

where $\boldsymbol{I}_{3N}$ is the $3N \times 3N$ identity matrix,

$$\boldsymbol{U} = (U(a^{(1)}), V(a^{(1)}), V'(a^{(1)}), \ldots, U(a^{(N)}), V(a^{(N)}), V'(a^{(N)}))^{\mathrm{T}},$$

$$\boldsymbol{D}_N(\omega) = [D_{ij}(\omega)]_{i,j=1}^{N}, \tag{20}$$

and

$$D_{ij}(\omega) = \begin{pmatrix} -\Psi_j(\omega)g(d_{ij}) & 0 & -\Pi_j(\omega)g(d_{ij}) \\ -\Pi_j(\omega)G'(d_{ij}) & \Phi_j(\omega)G(d_{ij}) & -\Upsilon_j(\omega)G'(d_{ij}) \\ -\Pi_j(\omega)G''(d_{ij}) & \Phi_j(\omega)G'(d_{ij}) & -\Upsilon_j(\omega)G''(d_{ij}) \end{pmatrix},$$

where $d_{ij} = a^{(i)} - a^{(j)}$. Note in the case when $i = j$, we have

$$D_{jj}(\omega) = \begin{pmatrix} -\dfrac{i\Psi_j(\omega)}{2EAk_R} & 0 & -\dfrac{i\Pi_j(\omega)}{2EAk_R} \\ 0 & \dfrac{(1-i)\Phi_j(\omega)}{4EJk_B^3} & 0 \\ -\dfrac{(1+i)\Pi_j(\omega)}{4EJk_B} & 0 & -\dfrac{(1+i)\Upsilon_j(\omega)}{4EJk_B} \end{pmatrix}. \tag{21}$$

A non-trivial solution $\boldsymbol{U}$ to (19) is then identified by considering the solutions of

$$\det(\boldsymbol{I}_{3N} + \omega^2 \boldsymbol{D}_N(\omega)) = 0.$$

4. Dynamic Green's functions and their derivatives in flexural scattering problems

Here, we aim to understand the behaviour of the beam with a single resonator attached ($N = 1$). In particular, we consider a flexural wave propagating along beam initiated remotely from the left and incident on the resonator. Without loss of generality, we assume the resonator is situated at the origin (that is $a^{(1)} = 0$). In this case, as we will see, the resonator can scatter the incoming wave, creating perturbations in the total displacement field. This interaction can result in the increase or reduction of the flexural wave amplitude in the system and promote the propagation of axial waveforms.

As an example of similar phenomena observed here, in Fig. 2, we show the response of the lateral beam attached to a resonator, which scatters an incoming wave of unit amplitude generated remotely from the left of the medium. Figure 2(a) shows the total displacement field of the problem based on the analytical formulation discussed in section 4.1. In this case, in comparing with the system without the resonator, this device can cause a slight amplification of the waves propagating to its left, owing to the presence of reflected flexural waves. On the other hand, transmitted waves caused by the resonator can reduce the amplitude of the wave propagating to the right.

Figure 2(b) illustrates the behaviour of the scattered field generated by the resonator based on finite element computations in COMSOL MultiPhysics 5.3. There the problem considered is programmed in the Structural Mechanics module. The lateral beam in the system is given a sufficiently large

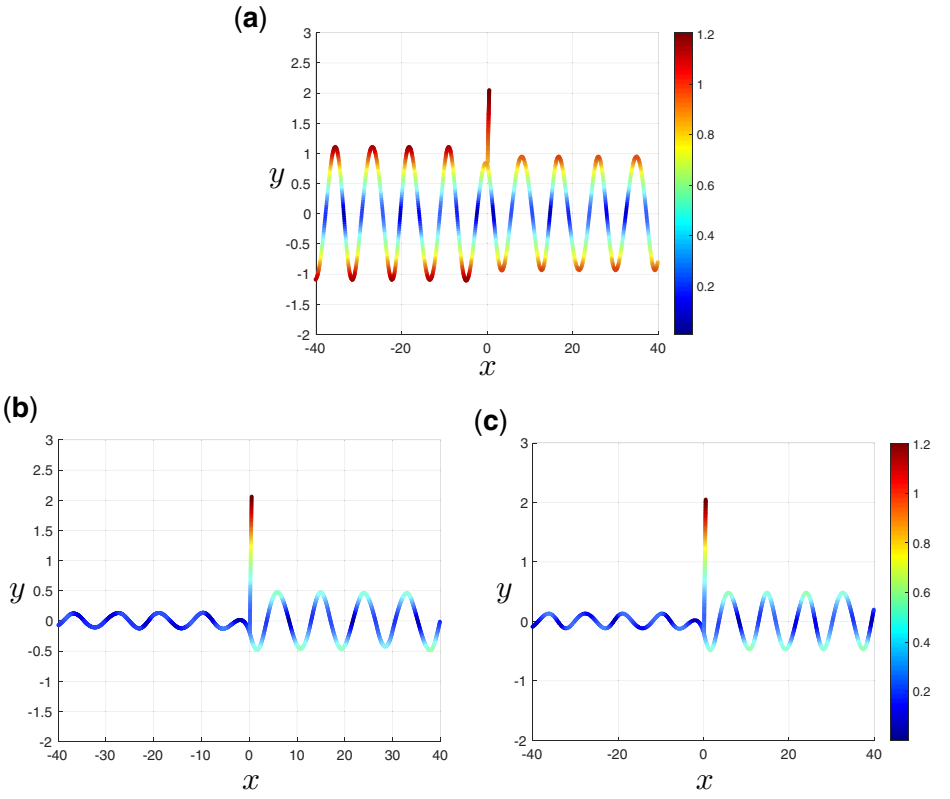

Fig. 2 (a) Total wave field produced by an incident wave of unit amplitude and frequency $1/(4\pi)$ interacting with a single flexural resonator. (b) Scattered wave field associated with the configuration in (a) determined by computations in COMSOL MultiPhysics 5.3. (c) The scattered wave field produced by the analytical solution is described in section 4.1. All other physical parameters in this computation are set to unity. The colour plot displays the total displacements within the medium.

length and absorbing layers are set at both its ends to mitigate the influence of reflections from these points.

It is evident in Fig. 2(b) that the flexural waves generated by the resonator dominate the scattering process. Contrary to the observations made in relation to Fig. 2(a), the waves to the right of the resonator have a much larger amplitude than those on the left and these waves possess different phases that allow the system to assume the response in Fig. 2(a) when combined with the incident wave.

In Fig. 2(c), we present the scattered field based on the analytical solution derived here. We note there is an excellent visual agreement between the computations shown in Fig. 2(b) and (c). Further examples of waveforms created by the resonator can be found in section 4.4 below, where the promotion of axial waves at the expense of flexural wave motion can occur.

4.1 *The scattering problem and its solution*

Based on section 2, the governing equations for the lateral beam are

$$\rho A\omega^2 U(x) + EAU''(x) = -\mathscr{Q}\delta(x), \tag{22}$$

and

$$-\rho A\omega^2 V(x) + EJV''''(x) = \mathscr{F}\delta(x) - \mathscr{M}\delta'(x), \tag{23}$$

for $-\infty < x < \infty$,

$$\begin{aligned}
\mathscr{Q} &= \omega^2\left[\Psi_1(\omega)U(0) + \Pi_1(\omega)V'(0)\right],\\
\mathscr{F} &= \omega^2\Phi_1(\omega)V(0),\\
\mathscr{M} &= \omega^2\left[\Pi_1(\omega)U(0) + \Upsilon_1(\omega)V'(0)\right].
\end{aligned}$$

In this scenario, similar to the derivation of (15), the axial motion and flexural motion of the beam possess the following amplitudes

$$U(x) = \omega^2\left[\Psi_1(\omega)U(0) + \Pi_1(\omega)V'(0)\right]g(x),$$

$$\begin{aligned}
V(x) = e^{ik_Bx} &- \omega^2\Phi_1(\omega)V(0)G(x)\\
&+\omega^2\left[\Pi_1(\omega)U(0) + \Upsilon_1(\omega)V'(0)\right]G'(x),
\end{aligned} \tag{24}$$

where we note the incident flexural field has been included in the representation of $V(x)$. The unknown coefficients $U(0)$, $V(0)$ and $V'(0)$ are then determined from an inhomogeneous system, found through following similar steps as in sections 3.1 and 3.2, that gives:

$$\boldsymbol{U} = (\boldsymbol{I}_3 + \omega^2\boldsymbol{\mathcal{D}}(\omega))^{-1}\boldsymbol{U}_0 \tag{25}$$

with

$$\boldsymbol{U} = (U(0), V(0), V'(0))^{\mathrm{T}}, \quad \boldsymbol{U}_0 = (0, 1, ik_B)^{\mathrm{T}},$$

and $\boldsymbol{\mathcal{D}} = \boldsymbol{D}_1(\omega)$ (see (20) and (21)).

4.2 *Energy distribution within the structure*

We now analyse how the resonator influences the partition of the incident wave energy in producing reflected and transmitted waves. To get a better understanding of this, we consider the rate of change of energy in the system by analysing the transient equivalent of the equations (22) and (23) that are written in the time-harmonic regime.

4.2.1 Derivation of the energy balance identity. Firstly, we rewrite equations (22) and (23) using $u(x,t) = U(x)e^{-i\omega t}$ and $v(x,t) = V(x)e^{-i\omega t}$ to obtain:

$$-\rho A\ddot{u}(x,t) + EAu''(x,t) + \mathscr{Q}e^{-i\omega t}\delta(x) = 0, \tag{26}$$

and

$$-\rho A\ddot{v}(x,t) - EJv''''(x,t) + [\mathscr{F}\delta(x) - \mathscr{M}\delta'(x)]e^{-i\omega t} = 0. \tag{27}$$

To this end, we take (26) and (27), multiply by $\overline{\dot{u}}$ and $\overline{\dot{v}}$, respectively. Next, we sum the obtained equations and integrate the result with respect to x from $-a$ to a with $a > 0$. For this integral, we apply a standard procedure using integration by parts and then take the real part of the result. In doing so, one can derive the identity:

$$\frac{\partial}{\partial t}\left(\int_{-a}^{a}\mathcal{E}_0 dx\right) - \mathrm{Re}\left(\int_{-a}^{a}\mathcal{R}\,dx\right) + \mathrm{Re}\left(\left[\mathcal{N}(x)\right]_{x=-a}^{x=a}\right) = 0, \tag{28}$$

where $\mathcal{E}_0$ is the energy density, that is, energy density per unit length of the wave guide, given by

$$\mathcal{E}_0 = \frac{1}{2}\left(\rho A(|\dot{v}|^2 + |\dot{u}|^2) + EJ|v''|^2 + EA|u'|^2\right),$$

$\mathcal{R}$ is power density having the form

$$\mathcal{R} = \left\{\mathscr{Q}\overline{\dot{u}(x,t)}\,\delta(x) + [\mathscr{F}\delta(x) - \mathscr{M}\delta'(x)]\overline{\dot{v}(x,t)}\right\}e^{-i\omega t}$$

and the energy flux $\mathcal{N}$ is

$$\mathcal{N} = -EAu'(x,t)\overline{\dot{u}(x,t)} + EJ[v'''(x,t)\overline{\dot{v}(x,t)} - v''(x,t)\overline{\dot{v}'(x,t)}].$$

Note that with complex representations of the displacements, $\mathcal{E}_0$ is time-independent, and hence the first term in (28) is zero. Further, the integral in the second term of (28) is purely imaginary. This can be seen by evaluating this integral and using (25) as follows:

$$\begin{aligned}\int_{-a}^{a}\mathcal{R}\,dx &= \{\mathscr{Q}\overline{\dot{u}(0,t)} + \mathscr{F}\overline{\dot{v}(0,t)} + \mathscr{M}\overline{\dot{v}'(0,t)}\}e^{-i\omega t},\\ &= i\omega^3\Big\{\Psi_1(\omega)|U(0)|^2 + \Phi_1(\omega)|V(0)|^2 + \Upsilon_1(\omega)|V'(0)|^2\\ &\quad +2\Pi_1(\omega)\mathrm{Re}(U(0)\overline{V'(0)})\Big\}.\end{aligned}$$

Thus, we have shown that (28) reduces to

$$\mathrm{Re}\left(\left[\mathcal{N}(x)\right]_{x=-a}^{x=a}\right) = 0, \tag{29}$$

that is, the energy propagating to the left and the right of the resonator is the same.

4.3 *Energetic relationships involving wave amplitudes*

Employing (24), we then find

$$\lim_{x\to+\infty}\mathcal{N}(x)=N_+(x)=2EJk_B^3\omega|T_F|^2+EAk_R\omega|T_A|^2, \tag{30}$$

and

$$\lim_{x\to-\infty}\mathcal{N}(x)=N_-(x)=2EJk_B^3\omega(1-|R_F|^2)-EAk_R\omega|R_A|^2, \tag{31}$$

with R_F and R_A (T_F and T_A) representing the amplitudes of reflected (transmitted) waves associated with the flexural and axial motion of waveguide, given by

$$R_F=\frac{1}{4EJk_B^3}\left[i\mathscr{F}-k_B\mathscr{M}\right],\qquad T_F=1+\frac{1}{4EJk_B^3}\left[i\mathscr{F}+k_B\mathscr{M}\right]$$

and

$$R_A=T_A=\frac{i\mathscr{Q}}{2EAk_R}. \tag{32}$$

In combining (29)–(32), we then obtain the following identity

$$1=\frac{Ak_R}{Jk_B^3}|T_A|^2+|R_F|^2+|T_F|^2. \tag{33}$$

Further, note that in the configuration without a resonator, the axial and flexural deformations are decoupled and only the incident flexural wave propagates throughout the medium. This wave possesses the energy flux

$$\mathcal{N}_{\text{inc}}=2EJk_B^3\omega.$$

The corresponding energy density for this wave is then given by

$$\mathscr{E}_{\text{inc}}=\frac{\mathcal{N}_{\text{inc}}}{v_g^F}=\sqrt{\rho AEJ}k_B^2\omega,$$

where $v_g^F=2\sqrt{EJ/(\rho A)}$ is the group velocity of the flexural wave. With this, identity (33) can then be rewritten as the following energy balance law for the waveguide with a resonator:

$$\mathscr{E}_{\text{inc}}=C\mathscr{E}_A+\mathscr{E}_R^F+\mathscr{E}_T^F, \tag{34}$$

where $\mathscr{E}_R^F$ ($\mathscr{E}_T^F$) is the energy density for the reflected (transmitted) flexural wave given by

$$\mathscr{E}_R^F=\sqrt{\rho AEJ}k_B^2\omega|R_F|^2,\qquad \mathscr{E}_T^F=\sqrt{\rho AEJ}k_B^2\omega|T_F|^2, \tag{35}$$

$\mathscr{E}_A$ is energy density for the scattered axial waves and C is a dimensionless coefficient:

$$\mathscr{E}_A=A\sqrt{E\rho}k_R\omega|T_A|^2,\qquad C=\left(\frac{EA}{J\rho\omega^2}\right)^{1/4}. \tag{36}$$

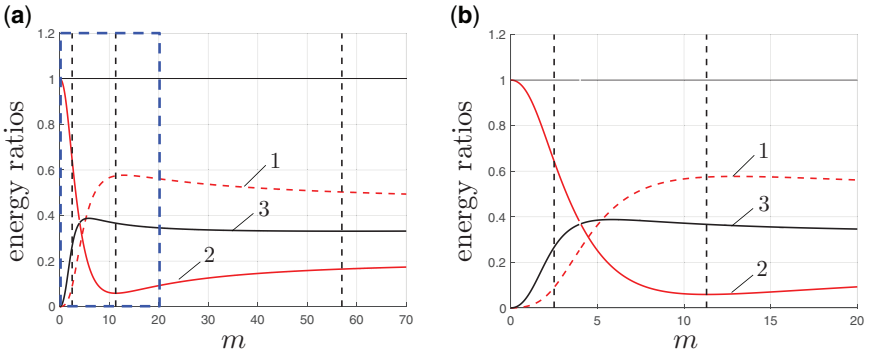

Fig. 3 (a) Energy ratios $\mathscr{E}_R^F/\mathscr{E}_{\rm inc}$ (curve labelled 1), $\mathscr{E}_T^F/\mathscr{E}_{\rm inc}$ (curve labelled 2) and $C\mathscr{E}_A/\mathscr{E}_{\rm inc}$ (curve labelled 3) as a function of the resonator mass m. (b) Magnification of the plot inside the blue dashed box in (a). Vertical black dashed lines correspond to the computations of the structure's profile in section 4.4.4. Computations are based on (35) and (36).

4.4 *Numerical illustrations for the scattering problem*

4.4.1 Numerical configuration. We consider a single massless flexural resonator possessing a spherical mass at the tip, having mass m, radius $r = 0.1$ and moment of inertia $I^z = \frac{2}{5}mr^2$. A wave of unit amplitude and frequency $\omega = 0.5$ is assumed to be incident on the resonator located at the origin. All other material parameters are set equal to unity in what follows. Our aim is to understand the effect of the changing resonator's mass on the propagation of the waves in lateral beam.

4.4.2 The energy balance. Here, we consider the behaviour in the partition of the incident wave energy density in accordance with (34) as we vary the resonator's mass. The associated results are presented in Fig. 3(a), where the influence of m on the energy ratios $\mathscr{E}_R^F/\mathscr{E}_{\rm inc}$, $\mathscr{E}_T^F/\mathscr{E}_{\rm inc}$ and $C\mathscr{E}_A/\mathscr{E}_{\rm inc}$ is illustrated. A magnification of the results in Fig. 3(a) are also provided in Fig. 3(b), to demonstrate fluctuations these ratios can undergo prior to converging to finite non-zero limits when increasing m.

If there is no mass at the tip of the resonator, the presence of the massless flexural element attached to the lateral beam has no influence on the incident wave Fig. 3(a) shows the resonator with a mass attached to its tip brings scattering effects. In this case, the incident wave energy is distributed amongst flexural and axial waves, propagating away from the resonator inside the lateral beam.

In particular, Fig. 3(a) and (b) reveals that the energy attributed to transmitted flexural wave can be minimised for an appropriate choice of the mass m (=11.3). Simultaneously, the energy density measured to the left of the resonator and attributed to flexural waves only is maximised at this value. Note these illustrations also show that the properties of the resonator can be tuned to allow the energy given to the axial wave propagating to the right of the resonator, given by $C\mathscr{E}_A/(2\mathscr{E}_{\rm inc})$, to be greater than the energy given to the transmitted flexural wave, represented by $\mathscr{E}_T^F/(\mathscr{E}_{\rm inc})$. In fact, this feature occurs for approximately $m > 6$, where at the start of this semi-infinite interval the energy possessed by the axial waves can be maximised.

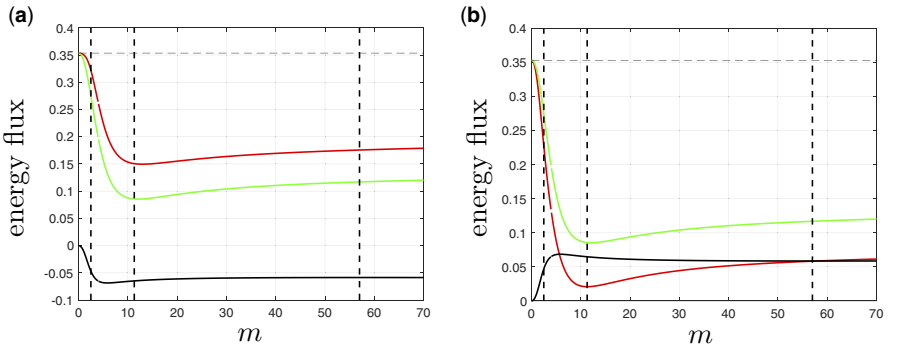

Fig. 4 (a) Energy flux as a function of the resonator's mass to the (a) left and (b) right of the resonator. The total energy flux in both cases is given by green curves, based on (30) and (31). The red (black) curves are the contributions to the flux generated by the flexural (axial) waves. Vertical black dashed lines occurring at $m = 2.5$, 11.3 and 57, correspond to the computations of the structure's profile in section 4.4.4. The horizontal dashed line represents the energy flux connected with the incident wave that propagates unperturbed through the system when $m = 0$, that is, when the mass of the flexural resonator is absent.

The above properties suggest that the axial deformations inside the medium can be become visible within the system (in contrast, for instance, Fig. 2 where axial wave deformations are suppressed), while effects due to the flexural deformations can be reduced. This effect amongst others is further investigated in section 4.4.4.

4.4.3 The energy fluxes induced by the resonator. Next, we illustrate the behaviour of the energy flux (that is, the rate of flow of energy through a cross section of the waveguide) in the medium in connection with the presence of the resonator.

First, we note that, in accordance with (29), Fig. 4(a) and (b) shows the total energy flux to the left and the right of the resonator are equal. However, both of these figures indicate the partition of these fluxes into fluxes attributed to flexural and axial waves are different to the left and right of the resonator.

When $m > 0$, Fig. 4(a) shows that on the left of the resonator the energy flux attributed to the combination of the incident and reflected flexural waves is always greater than the total flux. On the other hand, the flux connected with the axial waves propagating in this region is always negative, as expected due to the fact this is a feature of the outwardly propagating scattered field produced by the resonator. In correspondence with results in section 4.4.2 concerning the energy density in the medium, we note the resonator mass can be tuned to minimise the flux associated with both flexural waves and axial waves to the left of the resonator.

Figure 4(b) illustrates other special features of the waveforms produced by the resonator to its right. In this case, the flexural contribution to the energy flux, now generated by a single transmitted flexural wave is always smaller than the total flux. Further, the flux connected to the axial waveforms is positive. Figure 4(b) also demonstrates that the resonator can be tuned to promote the action of axial waves at the expense of flexural waves in this part of the system. In particular, the resonator mass may be tailored to minimise the flexural contribution to the energy density, so that the axial contribution is dominant, which is consistent with those results discussed in Fig. 3. This effect clearly

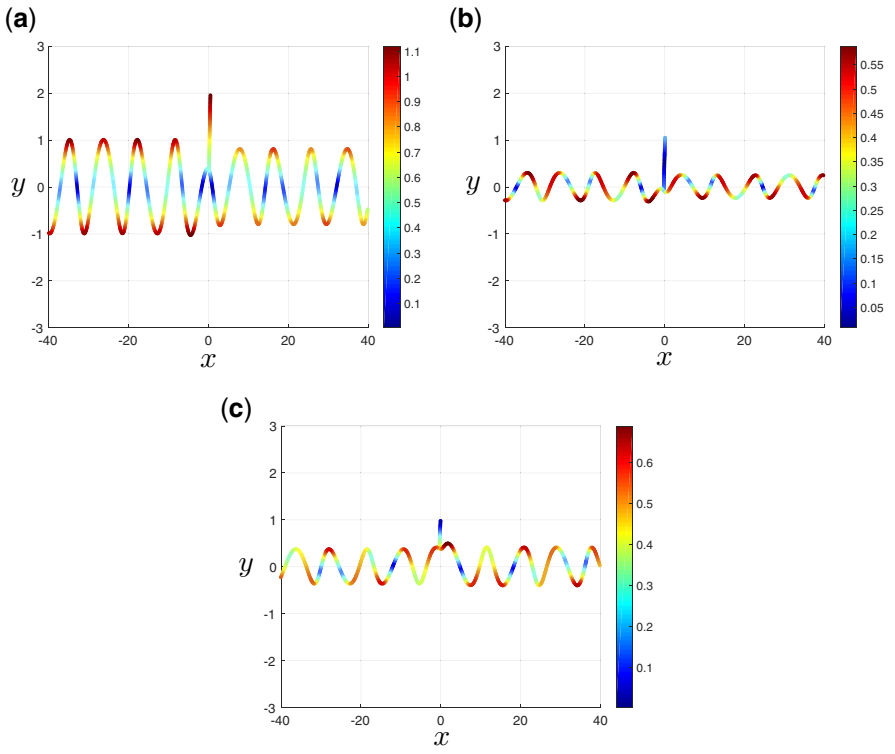

Fig. 5 Response of the lateral beam with different resonators having mass (a) 2.5, (b) 11.3 and (c) 57, that interact with an incident wave with unit amplitude and frequency $\omega = 0.5$. All other material parameters in this example are set equal to unity. The colour plot indicates the total displacements of the system.

occurs for a resonator whose mass satisfies $6 < m < 57$, where at the ends of this interval the fluxes for both wave types are approximately equal.

4.4.4 Structural response for different resonators. Here, we discuss the displacement profile assumed by the structure for different configurations of the resonators. These configurations correspond to the vertical dashed lines in Figs 3 and 4, for the cases when the resonator mass $m = 2.5$, 11.3 and 57. In ascending order, these values represent regimes when:

(i) the flexural waves are the dominant waveforms propagating in the lateral beam and the effects of the axial waves are small (see Fig. 5(a)),
(ii) when the transmitted axial waves carry more energy than the transmitted flexural waves and, in particular, the transmitted flexural wave energy can be minimised (Fig. 5(b)).
(iii) when flexural and axial transmitted waveforms possess the same amount of energy (Fig. 5(c)).

The profile of the structure for regime (i) is shown in Fig. 5(a). There, waves propagating through the medium are mainly of the flexural type and the resonator undergoes a significant deformation. The

axial response of the medium is suppressed, indicating the coupling between the axial and flexural deformations in this configuration is small. Additionally, it is evident the resonator enables a slight increase in the flexural wave amplitude to the left of the resonator, whilst producing a transmitted wave with a noticeable reduction in the wave amplitude.

In Fig. 5(b), we consider regime (ii), where the coupling between axial and flexural responses of the system becomes significant, and prominent axial effects are brought at the expense of flexural motion. Here, the displacements along the resonator are mostly small except at its connection to the lateral beam where a moderate deformation occurs. Despite these small deformations in the resonator, this passive system enables a significant reduction in the amplitude of the flexural wave propagating in the lateral beam either side of the resonator. Further, the influence of the axial waves in this medium is also clear, as the deformation produced does not represent a pure sinusoidal waveform (compare with Fig. 5(a)) and there is evidence of compression and extension in the lateral beam.

Regime (iii) is another case where the coupling between the axial and flexural motion is significant, but waveforms associated with both can carry similar amounts of energy. An example of such a regime is shown in Fig. 5(c). Here, we note the displacement of the resonator's base is significant relative to the displacements in the full medium. The influence of axial waves in the lateral beam is still visible but here the flexural wave amplitude is larger than that found in Fig. 5(b), which is consistent with the fact that in regime (iii), flexural waves possess more energy than those found in regime (ii).

4.5 *Scattering of flexural waves by N resonators*

Before moving to the next section, we briefly mention that the formulation presented in section 4.1 is easily extended to the case of N resonators. In this case, the total wavefields represented by $U(x)$ and $V(x)$ satisfy (1) and (2). For this problem, $U(x)$ takes the form in (15) and $V(x)$ admits the representation

$$V(x) = e^{ik_B x} - \sum_{1\le j\le N} \omega^2 \Phi_j(\omega) V(a^{(j)}) G(x - a^{(j)}) + \sum_{1\le j\le N} \omega^2 \left[\Pi_j(\omega) U(a^{(j)}) + \Upsilon_j(\omega) V'(a^{(j)}) \right] G'(x - a^{(j)}), \tag{37}$$

where the coefficients $U(a^{(j)})$, $V(a^{(j)})$ and $V'(a^{(j)})$, $1 \le j \le N$, are obtained via:

$$\boldsymbol{U} = (\boldsymbol{I}_{3N} + \omega^2 \boldsymbol{D}_N(\omega))^{-1} \boldsymbol{U}_0$$

with $\boldsymbol{D}_N(\omega)$ given in (20),

$$\boldsymbol{U} = (U(a^{(1)}), V(a^{(1)}), V'(a^{(1)}), \ldots, U(a^{(N)}), V(a^{(N)}), V'(a^{(N)}))^{\mathrm{T}},$$

and

$$\boldsymbol{U}_0 = (0, e^{ik_B a^{(1)}}, ik_B e^{ik_B a^{(1)}}, \ldots, 0, e^{ik_B a^{(N)}}, ik_B e^{ik_B a^{(N)}})^{\mathrm{T}}.$$

The solution described here will be implemented in numerical illustrations in the next section, where an effective model describing the case when N is large is derived as an efficient alternative to the solution presented here.

5. Dynamic homogenisation via meso-scale approximations

5.1 *Homogenisation of the governing equations*

Here, we derive the partial differential equations governing the effective behaviour of the medium in the case when the number of resonators within a finite interval of the comb multi-structure becomes large. The approximations are based on the exact meso-scale solution described above. This encodes important information about high-frequency dynamic regimes through Green's functions utilised in constructing the solution and the unknown coefficients characterising the motion of junctions obtained from the algebraic system. We note these coefficients for dense configurations are approximated by solutions to the corresponding effective problem, which is the generalised Rayleigh beam (see (**6**) for a similar related discussion), which in turn offers an efficient and fast method for solving a large algebraic system when the number of resonators is large.

To obtain the dynamic homogenisation approximation for the system, we will assume that N resonators occupy an interval $[0, l]$ and are separated by a distance $d_{ij} = d = l/N$, with $a^{(k)} = kd$, $k = 1, \ldots, N$. We also assume the resonators are identical and set:

$$L_j = L, \quad m_j = m = M/N, \quad I_j^z = I^z = aML^2/N, \tag{38}$$

where M and c represent the total mass and stiffness of the effective medium attached to the lateral beam. Additionally, concerning quantities associated with the axial motion and flexure of the resonators we let

$$E_jA_j = cL/N, \quad E_jJ_j = bcL^3/N, \qquad j = 1, \ldots, N. \tag{39}$$

Here, a and b refer to dimensionless parameters. The above leads to the following definitions:

$$\begin{aligned} \Psi_j(\omega) &= \frac{l}{N}\Psi_{\text{eff}}(\omega), \quad \Phi_j(\omega) = \frac{l}{N}\Phi_{\text{eff}}(\omega), \\ \Pi_j(\omega) &= \frac{l}{N}\Pi_{\text{eff}}(\omega), \quad \Upsilon_j(\omega) = \frac{l}{N}\Upsilon_{\text{eff}}(\omega), \end{aligned} \tag{40}$$

with

$$\begin{aligned} \Phi_{\text{eff}}(\omega) &= \frac{Mc}{l(c - M\omega^2)}, \quad \Psi_{\text{eff}}(\omega) = -\frac{12bcM(aM\omega^2 - bc)}{l\mathcal{D}}, \\ \Pi_{\text{eff}}(\omega) &= \frac{6bcML(aM\omega^2 - 2bc)}{l\mathcal{D}}, \quad \Upsilon_{\text{eff}}(\omega) = -\frac{4bcML^2(-3[1+a]bc + aM\omega^2)}{l\mathcal{D}} \end{aligned} \tag{41}$$

and

$$\mathcal{D} = aM^2\omega^4 - 4bc(1+3a)M\omega^2 + 12(bc)^2.$$

The effective equations for the medium can be obtained by taking the limit as $N \to \infty$ as follows.

Returning to (16) and (17), these equations take the form:

$$U(a^{(k)}) = \sum_{1 \le j \le N} \omega^2 d \left[\Psi_{\text{eff}}(\omega)U(a^{(j)}) + \Pi_{\text{eff}}(\omega)V'(a^{(j)})\right] g(a^{(k)} - a^{(j)})$$

$$V(a^{(k)}) = -\sum_{1\le j\le N} \omega^2 d\ \Phi_{\text{eff}}(\omega) V(a^{(j)}) G(a^{(k)} - a^{(j)}) + \sum_{1\le j\le N} \omega^2 d \left[\Pi_{\text{eff}}(\omega) U(a^{(j)}) + \Upsilon_{\text{eff}}(\omega) V'(a^{(j)})\right] G'(a^{(k)} - a^{(j)}).$$

Taking the limit as $N \to \infty, d \to 0$, one can replace the sums on the right-hand side by integrals over the interval from $[0, l]$ to retrieve:

$$U(x) = \omega^2 \int_0^l \left[\Psi_{\text{eff}}(\omega) U(\hat{x}) + \Pi_{\text{eff}}(\omega) V'(\hat{x})\right] g(x - \hat{x}) d\hat{x}$$

$$V(x) = -\omega^2 \int_0^l \Phi_{\text{eff}}(\omega) V(\hat{x}) G(x - \hat{x}) d\hat{x} + \omega^2 \int_0^l \left[\Pi_{\text{eff}}(\omega) U(\hat{x}) + \Upsilon_{\text{eff}}(\omega) V'(\hat{x})\right] G'(x - \hat{x}) d\hat{x}.$$

Next, one can utilise (13) and (14) after applying the differential operators connected with the axial and flexural problems of $U(x)$ and $V(x)$, respectively, that are now defined through the above integral equations. This yields the homogenised equations for the generalised Rayleigh beam:

$$\rho A \omega^2 U(x) + EAU''(x) = -\omega^2 \left[\Psi_{\text{eff}}(\omega) U(x) + \Pi_{\text{eff}}(\omega) V'(x)\right] \chi_{(0,l)}(x), \tag{42}$$

$$-\rho A \omega^2 V(x) + EJV''''(x) = \omega^2 \Phi_{\text{eff}}(\omega) V(x) \chi_{(0,l)}(x) - \omega^2 \left[\Pi_{\text{eff}}(\omega) U'(x) + \Upsilon_{\text{eff}}(\omega) V''(x)\right] \chi_{(0,l)}(x), \tag{43}$$

for $-\infty < x < \infty$, where $\chi_{(0,l)}(x)$ is the characteristic function of the set $(0, l)$. For the derivation of the natural boundary conditions of this effective model, see Appendix A. This is used next in combination with (42) and (43) to analyse the scattering effects of a dense periodic resonant cluster.

5.2 *Effective transmission problem*

Here, we consider the scattering of waves along the lateral beam that has infinite extent and contains a segment $[0, l]$ that is attached to the effective resonant layer. We assume a flexural wave of unit amplitude and frequency ω propagates from the far left of the lateral beam and interacts with the material situated in $[0, l]$. In this case, the total fields $U(x)$ and $V(x)$ are solutions of (42) and (43) and are assumed to satisfy the following transmission conditions

$$[U(x)]_{x=0} = [U(x)]_{x=l} = 0, \quad [U'(x)]_{x=0} = [U'(x)]_{x=l} = 0, \tag{44}$$

representing the jump in axial displacements and axial stress at $x = 0$ and l, which utilises the notation:

$$[W(x)]_{x=a} = W(x)\Big|_{x=a^+} - W(x)\Big|_{x=a^-}.$$

Additionally, we require transmission conditions for the flexural motion across the internal boundaries of the medium. More specifically, we impose the continuity of the flexural displacement, rotations and moments through:

$$[V(x)]\Big|_{x=0} = [V(x)]\Big|_{x=l} = 0, \qquad [V'(x)]\Big|_{x=0} = [V'(x)]\Big|_{x=l} = 0, \tag{45}$$

and

$$[V''(x)]\Big|_{x=0} = [V''(x)]\Big|_{x=l} = 0 \tag{46}$$

respectively. Further, we supply the following transmission conditions at $x = 0$ and $x = l$ concerning the shear forces:

$$EJV'''(x)\Big|_{x=0^-} = \{EJV'''(x) + \omega^2 \Pi_{\text{eff}}(\omega)U(x) + \omega^2 \Upsilon_{\text{eff}}(\omega)V'(x)\}\Big|_{x=0^+} \tag{47}$$

$$\{EJV'''(x) + \omega^2 \Pi_{\text{eff}}(\omega)U(x) + \omega^2 \Upsilon_{\text{eff}}(\omega)V'(x)\}\Big|_{x=l^-} = EJV'''(x)\Big|_{x=l^+}. \tag{48}$$

Note that here the forcing terms associated with the traces from within $[0, l]$ represent the natural boundary conditions appearing in the weak formulation of the effective problem. These effective shear forces are derived in Appendix A. In particular, in their representations, in addition to the standard third order derivatives associated with the internal shear force for an Euler–Bernoulli beam, there are terms corresponding to the effective input from the dense layer of resonators on top of the lateral beam. These terms correspond to the coupling effect already observed in the considered problem and rotational inertial terms that are sign indefinite.

5.2.1 The solution to the effective transmission problem. The solution to the effective problem described above takes the form:

$$U(x) = \begin{cases} B_1 e^{-ik_R x} & \text{if } x < 0, \\ \displaystyle\sum_{j=1}^{6} C_j e^{ik_j x} & \text{if } 0 < x < l, \\ B_2 e^{ik_R x} & \text{otherwise} \end{cases} \tag{49}$$

and

$$V(x) = \begin{cases} e^{ik_B x} + D_1 e^{-ik_B x} + D_2 e^{k_B x} & \text{if } x < 0, \\ \displaystyle\sum_{j=1}^{6} C_j \phi(k_j) e^{ik_j x} & \text{if } 0 < x < l, \\ D_3 e^{ik_B x} + D_4 e^{-k_B x} & \text{otherwise,} \end{cases} \tag{50}$$

where the first term in the representation of $V(x)$ for $x < 0$ represents the field incident on effective medium from the left.

In the above representation, k_j, $1 \leq j \leq 6$, are parameters governing the vibration response of the effective medium, which arrive from the solution of the algebraic equation:

$$E^2AJk^6 - E\omega^2(A[\rho J + \Upsilon_{\text{eff}}(\omega)] + J\Psi_{\text{eff}}(\omega))k^4 + \omega^2(\omega^2[\Pi_{\text{eff}}(\omega)^2 - \rho A\Upsilon_{\text{eff}}(\omega) - \Psi_{\text{eff}}(\omega)\Upsilon_{\text{eff}}(\omega)] + EA[\rho A + \Phi_{\text{eff}}(\omega)])k^2 - \omega^4(\rho A + \Psi_{\text{eff}}(\omega))(\rho A + \Phi_{\text{eff}}(\omega)) = 0. \tag{51}$$

We note that real solutions to this equation give effective wavenumbers for the medium in the segment $[0, l]$. Additionally, in (50),

$$\phi(k) = -\frac{ik\omega^2\Pi_{\text{eff}}(\omega)}{EJk^4 - \omega^2(\Upsilon_{\text{eff}}(\omega)k^2 + \rho A + \Phi_{\text{eff}}(\omega))}.$$

The 12 coefficients B_1, B_2, C_j, $1 \leq j \leq 6$, and D_i, $1 \leq i \leq 4$, can then be found by combining (49) and (50) with (44)–(48) and solving the corresponding algebraic system that results from this.

5.2.2 Efficiency of the dynamic homogenisation approximation in modelling dense resonator arrays. Here, we consider the efficiency of the solution to the effective scattering problem, presented in section 5.2.1, in predicting the response of the lateral beam in the case when the number of resonators within the system becomes large.

We assume a periodic distribution of N resonators within the interval $[0, 1]$ with properties as described in section 5.1. For the numerical computations presented here, the effective medium atop on the lateral beam (corresponding to the case when $N \to \infty$), is assumed to have mass $M = 10$, stiffness $c = 5$ and height $L = 1$. Additionally, we define the parameters $a = 1$ and $b = 1/4$, that appear in the definition of the resonator properties (38) and (39). The frequency of the incident wave is taken as $\omega = 0.88$.

Our aim here is to show the dynamic homogenisation approximation of section 5.2.1 can be used as an accurate alternative to the results of section 4.5, concerning the scattering of flexural waves by N resonators, when $N \to \infty$.

First, we demonstrate the accuracy of the results of section 4.5 in determining the dynamic behaviour of the lateral beam with a collection of N resonators. We focus the analysis on the scattered wave field obtained by removing the incident field from (37). Figure 6(a) shows a comparison between the displacement profiles for the lateral beam based on the results of (i) section 4.5 and (ii) COMSOL Multiphysics 5.3, for the case when the lateral beam possesses $N = 4$ resonators. Once more, the COMSOL computation has been developed in the Structural Mechanics module using a finite beam with adaptive absorbing layers prescribed at its left and right ends.

Figure 6(a) again demonstrates that the procedure developed in section 4.5 is highly accurate, with the profiles predicted by both analytical and numerical methods being almost indistinguishable. A magnification of the profiles in the vicinity of the resonators has been presented in Fig. 6(b) to illustrate the sharp change in the response of the system. While it is possible to observe some small deviations between the computations presented, the analytical procedure developed here remains accurate even when abrupt changes in the comb occur due to the action of the resonators.

In relation to Fig. 6(a) and (b), we recall that the resonators induce internal point forces and moments within the system, whose magnitude and direction are controlled by both the principal displacements of the main beam and also terms (41) featuring the competition between the resonator

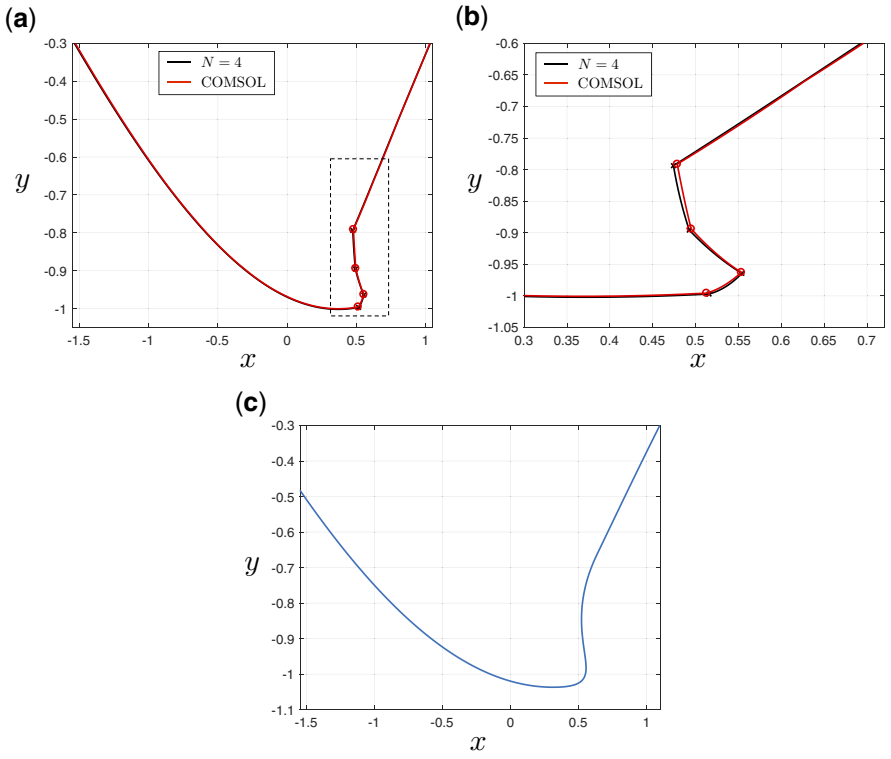

Fig. 6 (a) The response of the lateral beam attached to $N = 4$ equally spaced resonators. We show the profile corresponding to the scattered field produced when the incident wave interacts with the resonators. In (a), the computations are based on (i) the analytical solution discussed in section 4.5 and (ii) results from COMSOL MultiPhysics 5.3. The positions of the bases of individual resonators are represented by crosses and circles, respectively. (b) Magnification of the plot in the dashed square box of (a). (c) The profile of a beam with a dense cluster of equally spaced resonators in a segment. The response shown is based on the scattered field produced by the same incident field in (a) and (b) and obtained via homogenised solution presented in section 5.1.

properties with the vibration frequency. Those terms can alter the action of the additional translational and rotational inertial effects the resonators supply to the main beam at single points. The sign of the inertia terms may vary from individual resonator locations.

Further the resonators induce a coupling between the principal displacements, combining the motion of compressional waves with flexural waves. Hence, as a result of these factors, a range of complex motions can be supported by the main beam when influenced by the motion of the resonators.

This fact is further supported by the analysis of the asymptotic model found in section 5.2.1 for dense clusters. There, the solution to the problem depends on the roots of (51), which can be

1. real, providing typical waveforms within the dense cluster of resonators,
2. imaginary, giving evanescent longitudinal and flexural waves decaying to the left and the right within the segment of resonators, or

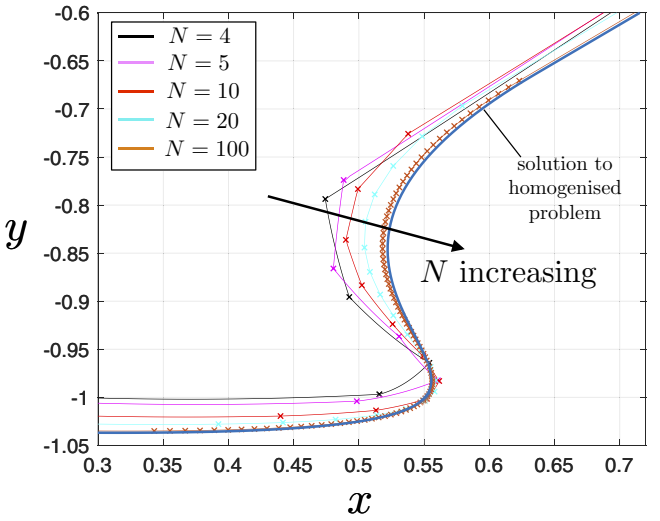

Fig. 7 Demonstration of the convergence of the scattered field with a periodic array of N resonators, based on results of section 4.5 for $N = 4, 5, 10, 20, 100$, to the solution of the effective dynamic problem of section 5.1 derived via the meso-scale solution (see also section 5.2.1). For the cases concerning the discrete array of resonators, the positions of the bases of the resonators are indicated by crosses along the corresponding profile.

3. complex, which are linked to oscillations with increasing or decreasing amplitude within the resonator cluster.

Here, the latter are not typically found in the study of undamped flexural and longitudinal waves for classical Euler–Bernoulli beams, whereas the penultimate waveform is only a feature of flexural wave motion in such systems. For the sake of brevity, here we will not explore the above described phenomena in detail.

Having verified the accuracy of the approach in section 4.5, we now consider the behaviour for the solution for case when $N \to \infty$. Recall in this limit, one should obtain the solution provided in section 5.1 to the effective dynamic problem (see also section 5.2.1). Figure 6(c) shows the behaviour of the solution to the problem obtained with a dynamic homogenisation based on the meso-scale solution. There the solution appears to be smooth in the sense there are no sharp changes in the profile as observed in Fig. 6 for a small collection of resonators. Simultaneously, the solution to the effective dynamic problem of section 5.1 reproduces similar features seen in Fig. 6(c).

In Fig. 7, we demonstrate the convergence of the solution (42) and (43) to the solution of the effective model obtained via the meso-scale solution as described in section 5.1 when $N \to \infty$. There it can be seen that for large N, the solution of the effective problem provides an excellent reproduction of the features in the behaviour of the lateral beam that possesses a large collection of resonators. The example presented illustrates that for large N, it is useful to consider the solution to the effective problem derived in section 5.1 in place of using the results of section 4.5, where the latter requires the solution of a large algebraic system that can be computationally intensive.

6. Finite meso-scale elastic combs: eigenvalue problems

In this section, we extend the methods developed in sections 3 and 5 to analyse the dynamic response of finite length multi-scale combs. In contrast with the previous sections, where the frequency of vibration is assumed to be known a priori, here we engage an eigenvalue problem as described in section 6.1. There the vibration modes and frequencies of the finite comb should be determined.

For the eigenvalue problem, we assume the comb is formed from finite lateral beam of length L_0 that is connected to a collection of N resonators. Without loss of generality, we consider the case when the ends of lateral beam are *clamped*. Further, we note that the method presented here is easily generalised to other constraints imposed on the ends of this beam.

The introduction of boundary points along the main beam brings new facets to the procedure of sections 3 and 5 where their influence should be taken into account and this is handled using dynamic Green's functions for a finite beam (see section 6.2).

Section 6.4 provides the comparison between the new algorithm developed in this section with benchmark finite element computations. This includes combs with a single resonator and a non-periodic array of resonators.

In section 6.5, we adopt the procedure of section 5 to develop the effective eigenvalue problem describing a finite multi-scale comb with a dense microstructure. There, based on this model, we also present computations highlighting the behaviour of the comb's eigenvalues as the denseness of its resonant microstructure increases.

6.1 *Eigenvalue problem for the finite comb multi-structure*

The boundary value problem now satisfied by the functions $U(x)$ and $V(x)$ describing axial and flexural motions, respectively, of a lateral beam of length L_0 involves (1) and (2), valid now for $0 < x < L_0$. It also consists of the boundary conditions:

$$U(0) = U(L_0) = 0 \tag{52}$$

for the axial deformation and

$$V(0) = V'(0) = V(L_0) = V'(L_0) = 0 \tag{53}$$

imposed on the flexural deformation.

6.2 *Dynamic Green's functions and the construction of the eigenmodes*

To identify the eigenfrequencies of the finite structure and the corresponding modes, one requires a representation of $U(x)$ and $V(x)$ that utilises the dynamic Green's functions for axial and flexural motions of the lateral beam, denoted by $g^{(0)}$ and $G^{(0)}$, respectively. These functions satisfy:

$$\rho A\omega^2 g^{(0)}(x,\hat{x}) + EA(g^{(0)})''(x,\hat{x}) + \delta(x-\hat{x}) = 0, \quad 0 < x, \hat{x} < L_0,$$
$$g^{(0)}(0,\hat{x}) = g^{(0)}(L_0,\hat{x}) = 0, \quad 0 < \hat{x} < L_0,$$

for the axial response and

$$-\rho A\omega^2 G^{(0)}(x,\hat{x}) + EJ(G^{(0)})''''(x,\hat{x}) + \delta(x-\hat{x}) = 0, \quad 0 < x, \hat{x} < L_0,$$

$$G^{(0)}(0,\hat{x}) = (G^{(0)})'(0,\hat{x}) = 0,$$
$$G^{(0)}(L_0,\hat{x}) = (G^{(0)})'(L_0,\hat{x}) = 0, \quad 0 < \hat{x} < L_0,$$

for the flexural response of the lateral beam when subjected to a unit point force acting in the x- and y-directions, respectively. These dynamic Green's functions are readily constructed explicitly and take the form:

$$g^{(0)}(x,\hat{x}) = \begin{cases} -\dfrac{\sin(k_R(L_0-\hat{x}))\sin(k_R x)}{k_R EA\sin(k_R L_0)}, & 0 < x \le \hat{x}, \\ -\dfrac{\sin(k_R(L_0-x))\sin(k_R \hat{x})}{k_R EA\sin(k_R L_0)}, & \hat{x} \le x < L_0, \end{cases} \tag{54}$$

and

$$G^{(0)}(x,\hat{x}) = \begin{cases} \dfrac{A_1(\hat{x})\mathcal{C}(x) + A_2(\hat{x})\mathcal{S}(x)}{4EJk_B^3(\cos(k_B L)\cosh(k_B L)-1)}, & 0 < x \le \hat{x} \\ \dfrac{A_1(x)\mathcal{C}(\hat{x}) + A_2(x)\mathcal{S}(\hat{x})}{4EJk_B^3(\cos(k_B L)\cosh(k_B L)-1)}, & \hat{x} \le x < L_0, \end{cases}$$

where

$$\mathcal{C}(x) = \cos(k_B x) - \cosh(k_B x), \quad \mathcal{S}(x) = \sin(k_B x) - \sinh(k_B x), \tag{55}$$

$$\begin{aligned} A_1(\hat{x}) = {} & \sinh(k_B L)\cos(k_B(L-\hat{x})) - \cosh(k_B L)\sin(k_B(L-\hat{x})) \\ & - \cos(k_B L)\sinh(k_B(L-\hat{x})) + \sin(k_B L)\cosh(k_B(L-\hat{x})) \\ & - \sin(k_B\hat{x}) - \sinh(k_B\hat{x}) \end{aligned}$$

and

$$\begin{aligned} A_2(\hat{x}) = {} & -\sin(k_B L)\sinh(k_B(L-\hat{x})) - \cos(k_B L)\cosh(k_B(L-\hat{x})) \\ & + \sinh(k_B L)\sin(k_B(L-\hat{x})) - \cosh(k_B L)\cos(k_B(L-\hat{x})) \\ & + \cos(k_B\hat{x}) + \cosh(k_B\hat{x}). \end{aligned}$$

6.2.1 Representation of eigenmodes. The solutions to (1), (2), (52) and (53) are then sought in the form

$$U(x) = \sum_{1\le j\le N} \omega^2 \left[\Psi_j(\omega)U(a^{(j)}) + \Pi_j(\omega)V'(a^{(j)})\right] g^{(0)}(x,a^{(j)}),$$

$$\begin{aligned} V(x) = {} & -\sum_{1\le j\le N} \omega^2 \Phi_j(\omega)V(a^{(j)})G^{(0)}(x,a^{(j)}) \\ & - \sum_{1\le j\le N} \omega^2 \left[\Pi_j(\omega)U(a^{(j)}) + \Upsilon_j(\omega)V'(a^{(j)})\right] G^{(0)}_{\hat{x}}(x,a^{(j)}). \end{aligned} \tag{56}$$

Note the derivative of Green's function in the last term in the above right-hand side (indicated by the subscript $\hat{x}$) is taken with respect to its second argument. This is to ensure the representation of $V(x)$ in (56) satisfies the boundary conditions imposed at the ends of the lateral beam (53). It remains to determine the quantities $U(a^{(j)})$, $V(a^{(j)})$ and $V'(a^{(j)})$ in the above solutions.

6.3 *Algebraic system for the unknown coefficients*

Proceeding in similar way to as outlined in section 3, we derive a system for the quantities $U(a^{(j)})$, $V(a^{(j)})$ and $V'(a^{(j)})$ in (56) the form:

$$(\boldsymbol{I}_{3N} + \omega^2 \boldsymbol{D}^{(0)}(\omega))\boldsymbol{U} = \boldsymbol{0}, \tag{57}$$

with

$$\boldsymbol{U} = (U(a^{(1)}), V(a^{(1)}), V'(a^{(1)}), \ldots, U(a^{(N)}), V(a^{(N)}), V'(a^{(N)}))^{\mathrm{T}},$$
$$\boldsymbol{D}^{(0)}(\omega) = [D_{ij}^{(0)}(\omega)]_{i,j=1}^{N},$$

and

$$D_{ij}^{(0)}(\omega) = \begin{pmatrix} -\Psi_j(\omega) g^{(0)}(a^{(i)}, a^{(j)}) & 0 & -\Pi_j(\omega) g^{(0)}(a^{(i)}, a^{(j)}) \\ \Pi_j(\omega) G_{\hat{x}}^{(0)}(a^{(i)}, a^{(j)}) & \Phi_j(\omega) G^{(0)}(a^{(i)}, a^{(j)}) & \Upsilon_j(\omega) G_{\hat{x}}^{(0)}(a^{(i)}, a^{(j)}) \\ \Pi_j(\omega) G_{x\hat{x}}^{(0)}(a^{(i)}, a^{(j)}) & \Phi_j(\omega) G_{x}^{(0)}(a^{(i)}, a^{(j)}) & \Upsilon_j(\omega) G_{x\hat{x}}^{(0)}(a^{(i)}, a^{(j)}) \end{pmatrix}.$$

Here, the subscripts appearing with the Green's functions refer to differentiation with respect to the indicated independent variables. The vector $\boldsymbol{U}$ in (57) is identified as a non-trivial solution of this system that corresponds to eigenfrequencies for the coefficient matrix of $\boldsymbol{U}$ is degenerate, that is, when:

$$\mathcal{K}_N = \det(\boldsymbol{I}_{3N} + \omega^2 \boldsymbol{D}^{(0)}(\omega)) = 0, \tag{58}$$

is satisfied.

6.4 *Numerical illustrations of eigenmodes*

In this section, we demonstrate the effectiveness of the procedure developed in sections 6.1–6.3 in predicting the eigenfrequencies and corresponding eigenmodes for the finite system.

6.4.1 The case of a single resonator. Firstly, we consider a finite system with a single resonator ($N = 1$), located midway along the lateral beam with length 2. All other physical parameters in the considered system are taken equal to unity. Predictions of the eigenfrequencies of this system are easily traced from (58). For the case $N = 1$, the plot of $\mathcal{K}_1$ as a function of the frequency $f = \omega/(2\pi)$ is given in Fig. 8(a). Here, the roots of this function (marked with black crosses) correspond to non-trivial solutions of (57) and consequently the eigenmodes are then determined from (56).

Predictions for the first 10 eigenfrequencies of the system based on the roots of (58) and those predicted in COMSOL are shown in Table 1. The results from both are almost indistinguishable. In this table, we also present the eigenvalues $f = n/2$, $n = 1, 2, \ldots$, that are linked to modes involving longitudinal deformations that do not excite flexural deformations (see section 6.4.2 for details). The first of these eigenfrequencies is shown in Fig. 8(a) by the red circle.

Figure 8(b) and (d) shows the first and sixth modes of the system based on computations within the finite element package COMSOL Multiphysics 5.3, which predicts the eigenfrequencies for these modes as $f = 0.121$ Hz and 0.89317 Hz. Figure 8(c) and (e) shows the first and sixth modes of the system computed with the analytical solution (56), which correspond to the frequencies

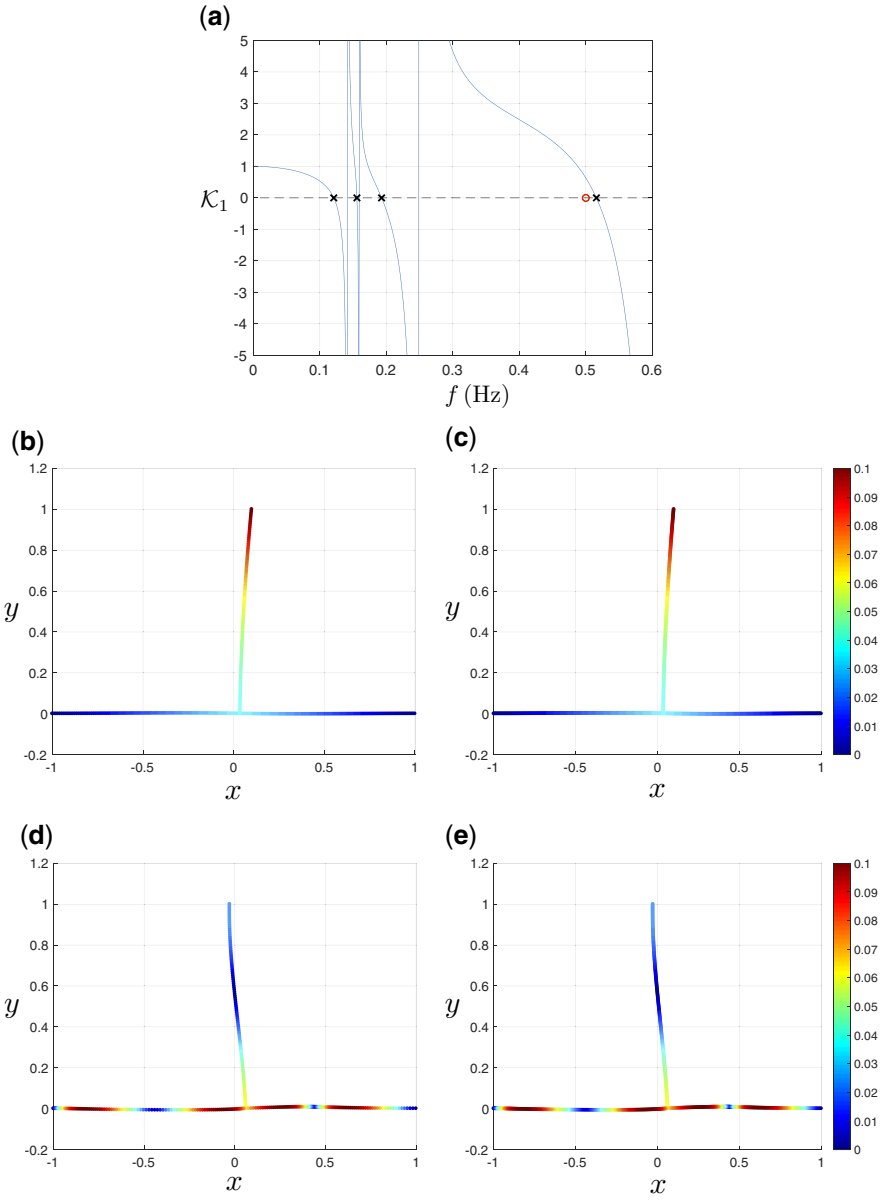

Fig. 8 (a) Plot of the function $\mathcal{K}_1$ as a function of the frequency $f = \omega/(2\pi)$ Hz based on the right-hand side of (58). The first eigenmode of the system with a single resonator is shown in (b) and (c). In (d) and (e), we show the sixth eigenmode of this system. Here, (b) and (d) are generated with COMSOL MultiPhysics 5.3 and (c) and (e) are based on the analytical solutions (56). The colour plots in (b)–(e) correspond to the total displacement of the medium.

Table 1 The eigenfrequencies for the first 10 modes of the heavy beam attached to a single resonator considered in section 6.4.1. Second column shows the results based on the roots of (58) and results of section 6.4.2 and the third column shows the predictions based on COMSOL MultiPhysics 5.3

	Eigenfrequency (Hz)	
Mode	Analytical (discrete meso-scale)	COMSOL
1	0.121	0.121
2	0.15584	0.15584
3	0.19294	0.19294
4	0.5	0.5001
5	0.5160	0.5161
6	0.8927	0.89317
7	0.9085	0.9085
8	1	1.001
9	1.3369	1.3384
10	1.5	1.5022

$f = 0.121$ Hz and 0.89275 Hz (the first of these indicated as a root in Figure 8(a)). Thus, based on Figure 8(b)–(e), we can conclude there is an excellent agreement for the computations of eigenmodes and corresponding eigenfrequencies between those produced by COMSOL MultiPhysics 5.3 and the analytical procedure developed in sections 6.2 and 6.3.

Figure 8(b) and (c) shows the first mode of the system can produce a localised excitation only in the resonator of the system, whereas Fig. 8(d) and (e) demonstrates the sixth mode may correspond to a significant excitation of the lateral beam. We note that these effects are dependent on the material parameters and different responses and values of the eigenfrequencies may be obtained with a different choice of material parameters, where effects attributed to negative inertial terms in (1) and (2) may play a significant role.

6.4.2 Longitudinal vibration degeneracy. In addition to the above discussed eigenmodes for the case of a single resonator, where a combination of flexural and longitudinal deformations can appear, we note there exist modes at where these responses can decouple. These particular modes are linked to a degeneracy of the meso-scale representation (56). Indeed, at frequencies where the decoupling effect occurs, the meso-scale representation (56) for the axial displacement is no longer valid as the Green's function $g^{(0)}$ in (54) is singular. The resulting modes of the medium correspond to when the flexural deformation is absent, that is, $V(x) \equiv 0$ and the axial deformation possesses a node at the junction point $x = L_0/2$. Specifically, the axial deformation has the form

$$U(x) = B \sin\left(\sqrt{\frac{\rho}{E}}\omega^{(j)}x\right), \qquad \omega^{(j)} = 2\sqrt{\frac{E}{\rho}}\frac{\pi j}{L_0}, \quad j = 1, 2, \ldots, \tag{59}$$

where B is a displacement amplitude and the eigenfrequencies $\omega^{(j)}$, $j = 1, 2, \ldots$, specified are singular points of (54). Here, (59) are a subset of the solutions to the classical problem for longitudinal

vibration modes of a finite rod that satisfy:

$$\rho A\omega^2 U(x) + EAU''(x) = 0, \qquad 0 < x < L_0,$$

together with (52). Note according to (59), at the junction point of the medium we have $U(L_0/2) = 0$ and (59) together with $V(x) \equiv 0$ satisfy (1), (2), (52) and (53).

6.4.3 Non-periodic arrays of resonators. Here, we analyse the effectiveness of the analytical procedure, constructed in sections 6.1–6.3, when used to predict the eigenfrequencies and associated eigenmodes of a system possessing a non-periodic array of multiple resonators.

We consider an array of resonators with masses given by spheres, with radius $r_j = 0.1$, mass $m_j = 0.2j$ and rotational inertia $I^z = \frac{2}{5} m_j r_j^2$, $1 \le j \le N$, and attached to the lateral beam of length 2. The position of the bases of the resonators along the lateral beam are chosen in a non-periodic fashion having a spacing between neighbouring resonators of either 0.1 or 0.05. Additionally, the lengths of the individual resonators can vary, taking a value of 1 or 0.5. All other material parameters of the system are taken as unity.

Figure 9(a) shows the first mode of the system generated by COMSOL MultiPhysics 5.3, which corresponds to the eigenfrequency $f = 0.072471$ Hz. Here, an eigenfrequency analysis has been implemented in the Structural Mechanics module to produce this associated computation. For this vibration mode, the deformation is localised within the non-periodic resonator array, while outside of this array the lateral beam remains undisturbed. The 24th mode of the system, whose eigenfrequency is $f = 1.0876$ Hz, determined via COMSOL MultiPhysics 5.3 can be found in Fig. 9(c). In this example, the higher mode frequency results in a high deformation of the lateral beam that also engages the motion of the lower portion of the resonator array. We note the displacements of the tips of the resonators are relatively small at this frequency regime.

Figure 9(b) and (d) presents the computations based on the analytical results (56), which computes the eigenfrequencies of these modes to be $f = 0.072471$ Hz and $f = 1.0872$Hz, respectively. Once again we observe an excellent agreement between the modes computed in Fig. 9(a) and (c) with the finite element method and those in Fig. 9(b) and (d) based on the analytical method developed in this article.

In the case when the resonator number becomes very large, the computation of eigenfrequencies and eigenmodes through numerical means can become laborious and difficult to compute accurately. In this case, the method presented in here provides an efficient alternative to computing these quantities.

6.5 *Effective eigenvalue problem for large N*

Here, we discuss an effective eigenvalue problem that can be obtained from following the procedure developed in section 5.1. In the low-frequency regime, this eigenvalue problem describes the dynamic behaviour of the finite beam, clamped at both ends and with an internal segment attached to a large array of periodically placed flexural resonators.

To retrieve this effective problem, we consider a periodic array of resonators attached to the lateral beam, contained within an interval $[l_1, l_2] \subset [0, L]$, with positions

$$a^{(j)} = l_1 + j(l_2 - l_1)/(N + 1), j = 1, \dots, N.$$

The remaining material parameters are as described in section 5.1.

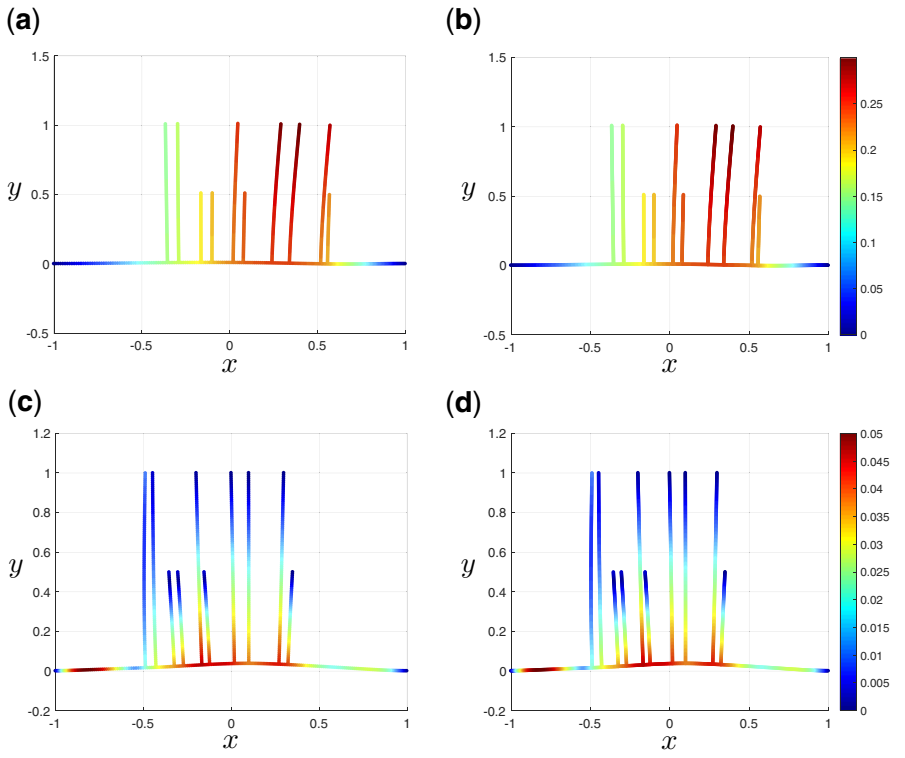

Fig. 9 Eigenmodes for the first and 24th modes of a comb possessing a non-periodic array of resonators. Here, (a, c) are computed using COMSOL MultiPhysics 5.3 and (b, d) are produced with the formulae in (56). The colour plot in (a)–(d) shows the total displacements assumed by the structure at the determined eigenfrequencies.

In this case, one may follow a similar approach as in section 5.1 using (56) and the subsequent algebraic system formed for the unknown coefficients in the right-hand side by taking $x = a^{(j)}$, $1 \leq j \leq N$. Then, allowing $N \to \infty$, we recover an effective eigenvalue problem involving displacement functions $U(x)$, $V(x)$ that is formed from (42), (43), the clamping conditions (52), (53) and the effective transmission conditions (45)–(48) (with $x = 0, l$ replaced with l_1 and l_2, respectively), representing the interaction between segments of the lateral beam with and without resonators.

The non-trivial solution of the effective eigenvalue problem is then sought in the form

$$U(x) = \begin{cases} B_1 \sin(k_R x) & \text{if } 0 < x < l_l, \\ \displaystyle\sum_{j=1}^{6} C_j e^{ik_j x} & \text{if } l_1 < x < l_2, \\ B_2 \sin(k_R(x - L)) & \text{if } l_2 < x < L. \end{cases} \tag{60}$$

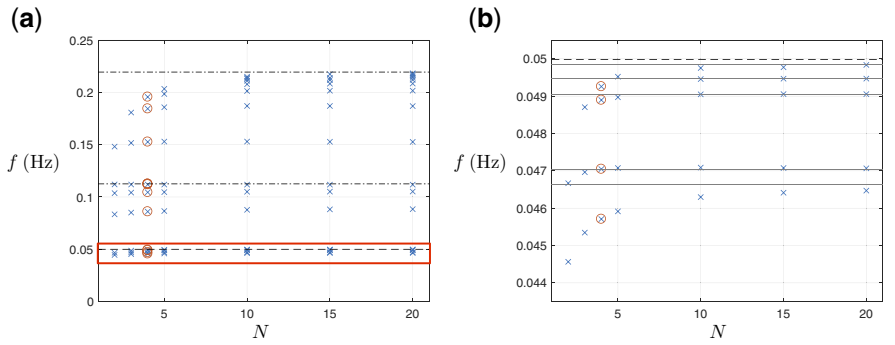

Fig. 10 Eigenvalues of the comb as a function of N. (a) The eigenvalues of the comb found using the method of sections 6.2.1–6.3 and the degeneracies of the system (58), represented by crosses. (b) Magnification of the plot within the red box found in (a). There, horizontal dashed and dot-dashed lines correspond to the resonant frequencies for the axial and flexural motions of the resonators, respectively. The horizontal solid lines coincide with the eigenvalues obtained via the dynamic homogenisation approximation of section 6.5 based on the meso-scale solution presented here. Additionally, we present computations for the eigenfrequencies for $N = 4$, computed via COMSOL MultiPhysics 5.3 and shown as red circles.

and

$$V(x) = \begin{cases} D_1\mathcal{C}(x) + D_2\mathcal{S}(x) & \text{if } 0 < x < l_1, \\ \displaystyle\sum_{j=1}^{6} C_j\phi(k_j)e^{ik_j x} & \text{if } l_1 < x < l_2, \\ D_3\mathcal{C}(x-L) + D_4\mathcal{S}(x-L) & \text{if } l_2 < x < L, \end{cases} \tag{61}$$

where $\mathcal{C}$ and $\mathcal{S}$ are defined in (55) and the frequency dependent parameters k_j, $1 \le j \le 6$, are found as solutions of (51). In addition, coefficients B_j, $j = 1, 2$, D_j, $1 \le j \le 4$ and C_j, $1 \le j \le 6$, are found from a homogeneous system by inserting (60) and (61) into the boundary conditions and transmission conditions for the effective problem. In doing so, one may also find the corresponding effective eigenfrequencies through the degeneracies of the homogeneous system.

6.6 *The behaviour of eigenfrequencies for large N*

In this section, we investigate the behaviour of the eigenvalues of a beam attached to a periodic array of resonators as their number N is increased. We consider the lateral beam having length $L = 2$, and with $E = J = A = \rho = 1$. The resonators have the material properties outlined in section 6.5, where the effective mass of the resonant medium obtained in the limit as $N \to \infty$ is $M = 10$, its stiffness is $c = 5$ and the parameters $a = 1$ and $b = 1/4$.

Using the theory developed in section 6.5, Fig. 10 illustrates the behaviour of eigenvalues for the considered configuration in the low frequency regime as a function of the total number N of the resonators. Figure 10(a) demonstrates that as N increases, the number of eigenvalues in the considered frequency interval $0 \le f \le 0.25$ can increase. In particular, the spacing between the frequencies can vary, with eigenvalues clustering near the axial and flexural resonant frequencies of the resonators.

In Fig. 10(a), we have also verified the computations produced by the theoretical results for the case $N = 4$, that once more demonstrates an excellent agreement between the computations based on the analytical results here and the method of finite elements employed by COMSOL MultiPhysics 5.3.

A closer inspection of the eigenvalues in the lowest frequency regime, which are bounded above by the axial resonant frequency of individual resonators, is provided in Fig. 10(b). The natural frequencies of the resonators act as accumulation points for eigenfrequencies of the entire system for large N. Additionally, we demonstrate the convergence of the eigenfrequencies, predicted by the method of sections 6.2.1 and 6.3, to those obtained from the dynamic homogenisation approximation discussed in section 6.5 that is traced from the meso-scale solution. This example once again illustrates the benefit of using the effective boundary value problem in place of handling the analytical procedure of sections 6.2.1 and 6.3 that utilises the manipulation of a large algebraic system when $N \to \infty$. Finally, we note once more that, as demonstrated earlier, the number of eigenfrequencies within a given interval can grow with increase of N. Hence, one can expect the model of section 6.5 to not only provide a good approximation to the eigenvalues for systems with a sufficiently large number of resonators but also to reveal additional eigenvalues connected with the effective medium. This fact has been verified numerically using the results of section 6.5 and is not presented here.

7. Reduction to the Rayleigh beam

We conclude the work presented here by discussing how one can tune or modify the comb multi-structure considered above to approximate the behaviour of a Rayleigh beam (**58**) that possesses negative translational and rotational inertia. We note that the equation for a Rayleigh beam was derived in (**25**) by considering the low-frequency approximation to an infinite symmetric flexural structure formed from periodically placed masses connected by massless beams. In a similar spirit, and for simplicity, here we consider a structure of infinite extent with periodically placed identical resonators, as described in section 5. Our goal is to recover an effective equation for the Rayleigh beam inside the interval $(0, l)$. In reproducing the behaviour of a Rayleigh beam in this region, one seeks the equation that governs the flexural displacement $V(x)$ in the form:

$$-\omega^2 \mathcal{R}(\omega) V(x) + EJV''''(x) + \omega^2 \mathcal{J}(\omega) V''(x) = 0, \qquad 0 < x < l \tag{62}$$

where the transverse displacement $V(x)$ is no longer coupled with the axial displacement $U(x)$. Additionally, here $\mathcal{R}$ and $\mathcal{J}$ are sign-indefinite terms depending on the radian frequency of vibration. These coefficients contribute to determining the magnitude and direction of the displacement and rotational inertia of the medium. Our goal here is to illustrate two approaches to determine the functions $\mathcal{R}$ and $\mathcal{J}$ using the theory developed in this article, consequently producing design methods to retrieve the behaviour of a Rayleigh beam with either negative displacement or negative rotational inertia.

7.1 *Frequency specific behaviour analogous to the Rayleigh beam*

Our first approach in recovering (62) involves a straight-forward application of the theory developed in sections 2 and 5 in considering the comb in Fig. 11(a). We recall that in this model the flexural resonators considered induce a coupling of axial and flexural motions of the lateral beam. Hence, one needs to identify ways to eliminate this effect to successfully retrieve the Rayleigh beam.

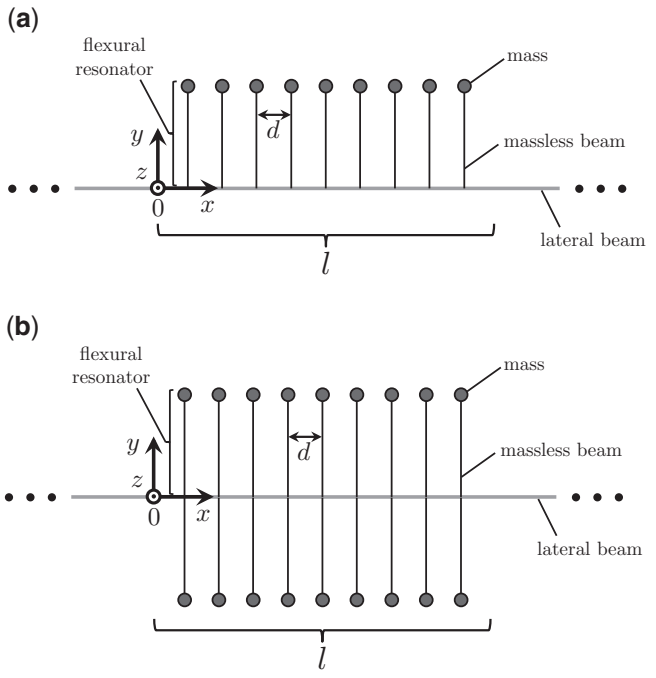

Fig. 11 Two flexural systems that replicate the behaviour of the Rayleigh beam in the low-frequency regime. (a) A periodic system analogous to the systems considered in sections 2–5, where resonators couple the flexural and axial displacements of the lateral beam except at a particular frequency. (b) A system symmetric with respect to the lateral beam, where such a coupling is absent due to geometrical considerations.

Following section 2, it is possible to write the equations of motion for the system shown in Fig. 11(a) as (1) and (2).

$$\rho A\omega^2 U(x) + EAU''(x) = \\ -\sum_{1\le j\le N} \omega^2 d\left[\Psi_{\text{eff}}(\omega)U(a^{(j)}) + \Pi_{\text{eff}}(\omega)V'(a^{(j)})\right]\delta(x-a^{(j)}), \tag{63}$$

and

$$-\rho A\omega^2 V(x) + EJV''''(x) = \sum_{1\le j\le N} \omega^2 d\Phi_{\text{eff}}(\omega)V(a^{(j)})\delta(x-a^{(j)}) \\ -\sum_{1\le j\le N} \omega^2 d\left[\Pi_{\text{eff}}(\omega)U(a^{(j)}) + \Upsilon_{\text{eff}}(\omega)V'(a^{(j)})\right]\delta'(x-a^{(j)}), \tag{64}$$

for $-\infty < x < \infty$, where Ψ_{eff}, Φ_{eff}, Υ_{eff} and Π_{eff} are defined in (41). As before, this model embeds a frequency dependent coupling governed by the appearance of rational functions in terms of the

frequency parameter. On inspection of these equations, one sees that for the coupling of the flexural and axial displacements to be eliminated, we require $\Pi_{\text{eff}}(\omega_{\text{RB}}) = 0$, where ω_{RB} is the frequency that allows the considered system to reproduce the motion of the Rayleigh beam. According to (3), this immediately leads to the conclusion that the frequency should be chosen as

$$\omega = \omega_{\text{RB}} = \sqrt{\frac{EJ}{LI^z}} = \sqrt{\frac{2bc}{aM}}, \tag{65}$$

where a, b and c are dimensionless parameters associated with the material properties of the resonant material obtained as $N \to \infty$ within $[0, l]$. In this case, the axial displacement $U(x)$ decouples from the flexural displacement of the system $V(x)$ in (63) and (64) embedding the influence of resonators at certain points along the beam.

Next, assuming the frequency is chosen as in (65), we write the flexural displacement as the solution of (64) as:

$$V(x) = -\sum_{1\le j\le N} \omega_{\text{RB}}^2 \Big\{ \Phi_{\text{eff}}(\omega_{\text{RB}}) V(a^{(j)}) G(x - a^{(j)}) - \Upsilon_{\text{eff}}(\omega_{\text{RB}}) V'(a^{(j)}) G'(x - a^{(j)}) \Big\} d. \tag{66}$$

we can derive an analogous equation to (62) by following a similar the procedure to section 5. This leads to the expressions governing the displacement and rotational inertia as

$$\mathcal{R}(\omega) = \rho A + \Phi_{\text{eff}}(\omega), \qquad \mathcal{J}(\omega) = \Upsilon_{\text{eff}}(\omega),$$

respectively, where it is apparent the resonator properties may be chosen to adjust the sign of these terms, leading to negative translational and rotational inertial effects in (62).

7.2 *Constructing a Rayleigh beam with a symmetric multi-structure*

We now consider the structure in Fig. 11(b), which is symmetric about the x-axis, and demonstrate how one can recreate the behaviour of a Rayleigh beam with this system.

In modelling the system in this case, (4) and (5) are updated to

$$\rho A\omega^2 U(x) + EAU''(x) = \sum_{1\le j\le N} (\mathcal{Q}_-^{(x,j)} - \mathcal{Q}_+^{(x,j)}) \delta(x - a^{(j)}), \tag{67}$$

$$-\rho A\omega^2 V(x) + EJV''''(x) = \sum_{1\le j\le N} (\mathcal{F}_-^{(y,j)} - \mathcal{F}_+^{(y,j)}) \delta(x - a^{(j)}) + \sum_{1\le j\le N} (\mathcal{M}_-^{(z,j)} - \mathcal{M}_+^{(z,j)}) \frac{d}{dx} \delta(x - a^{(j)}), \tag{68}$$

where $-\infty < x < \infty$. In these equations, the terms $\mathcal{M}_+^{(z,j)}$ and $\mathcal{Q}_+^{(x,j)}$, represent the bending moments and shear forces supplied by the jth, $1 \le j \le N$, resonator located above the lateral beam and having

the form:

$$\mathcal{Q}_+^{(x,j)} = \omega^2 \Psi_{\text{eff}}(\omega) U(a^{(j)}) d + \omega^2 \Pi_{\text{eff}}(\omega) V'(a^{(j)}) d,$$

$$\mathcal{M}_+^{(z,j)} = \omega^2 \Pi_{\text{eff}}(\omega) U(a^{(j)}) d + \omega^2 \Upsilon_{\text{eff}}(\omega) V'(a^{(j)}) d,$$

where these have been derived by combining the right-hand sides of (12) with (38) and (39). Similarly, $\mathcal{F}_+^{(y,j)}$ are the axial forces produced by the same elements that influence the lateral beam, which based on (8) and section 5 are:

$$\mathcal{F}_+^{(y,j)} = \omega^2 \Phi_{\text{eff}}(\omega) V(a^{(j)}) d.$$

For the resonators situated below the symmetry axis of the system, one should calculate the axial forces $\mathcal{F}_-^{(y,j)}$, bending moments $\mathcal{M}_+^{(z,j)}$ and shear forces $\mathcal{Q}_+^{(x,j)}$ produced by these resonators at their connection to the lateral beam. The expressions for these forces are given by

$$\begin{aligned} \mathcal{Q}_-^{(x,j)} &= -\omega^2 \Psi_{\text{eff}}(\omega) U(a^{(j)}) d + \omega^2 \Pi_{\text{eff}}(\omega) V'(a^{(j)}) d, \\ \mathcal{M}_-^{(z,j)} &= \omega^2 \Pi_{\text{eff}}(\omega) U(a^{(j)}) d - \omega^2 \Upsilon_{\text{eff}}(\omega) V'(a^{(j)}) d \end{aligned} \tag{69}$$

and

$$\mathcal{F}_-^{(y,j)} = -\omega^2 \Phi_{\text{eff}}(\omega) V(a^{(j)}) d, \tag{70}$$

where details of their derivations can be found in the Appendix B.

Using the above, (67) and (68) then gives the following decoupled problem, involving an equation for the axial motion of the beam:

$$\rho A \omega^2 U(x) + EAU''(x) = -2\omega^2 d \sum_{1 \le j \le N} \Psi_{\text{eff}}(\omega) U(a^{(j)}) \delta(x - a^{(j)}),$$

and the equation associated with flexural motion of the beam:

$$\begin{aligned} -\rho A \omega^2 V(x) + EJV''''(x) = &-2\omega^2 d \sum_{1 \le j \le N} \Phi_{\text{eff}}(\omega) V(a^{(j)}) \delta(x - a^{(j)}) \\ &-2\omega^2 d \sum_{1 \le j \le N} \Upsilon_{\text{eff}}(\omega) V'(a^{(j)}) \frac{d}{dx} \delta(x - a^{(j)}). \end{aligned}$$

The flexural displacement $V(x)$ can be determined in a similar way to (66) and it remains to utilise this solution to recover an effective problem related to the flexural behaviour of the beam within the segment $(0, l)$. Once more we follow a similar approach to section 5 and obtain the effective equation (62) for the flexure of the lateral beam, only now

$$\mathcal{R}(\omega) = \rho A + 2\Phi_{\text{eff}}(\omega), \qquad \mathcal{J}(\omega) = 2\Upsilon_{\text{eff}}(\omega),$$

dictate the displacement and rotational inertia, respectively, of the beam.

8. Conclusions

Here, we have analysed the dynamic behaviour of various flexural systems formed from a heavy beam attached to an array of non-periodically situated resonators. The resonators provide axial and flexural forcing to the heavy beam. This is reflected in the appearance of Dirac delta functions in the governing equations for the beam that are situated at the resonator sites. Additionally, the resonant elements supply the point moments to the main beam, bringing in additional forcing terms in governing equations of the beam in the form of the derivatives of delta functions. These forcing terms couple the axial and flexural motions of the main beam leading to a vectorial problem involving mixed order partial differential equations that should be solved to determine the motion of the system.

Naturally, the appearance of singular terms in the derived problem leads to the construction of exact solutions for the axial and flexural displacements in terms of Green's functions and their derivatives. Additionally, the solutions contain unknown intensities for the Green's functions that must be determined by solving a linear algebraic system linking the interaction of individual resonators within the system. The solutions provide a point-wise description of the motion of the beam, which includes the accurate characterisation of its response inside the resonant array at resonator sites and in between these locations. Further, the functions determining the displacements can treat meso-scale type scenarios, handling sparse resonator arrays, dense clusters of resonators and at low frequencies, giving effective descriptions of the medium in such configurations.

For problems involving infinite structures, we have analysed the scattering of waves resulting from the interaction of a remotely generated incident wave, having specified amplitude and frequency, with the resonant array. This problem leads to an inhomogeneous linear system appearing in the solutions that should be solved to determine the unknown intensities.

In contrast, when the beam is finite, one searches for eigenfrequencies and the corresponding eigenfunctions for the beam. In the corresponding derived solution, the intensities of the Green's functions result from non-trivial solutions of a homogeneous linear system that is degenerate at eigenfrequencies of the system.

We have also demonstrated the method provided here can be used to derive efficient dynamic homogenisation approximations that lead to an accurate description of the beam's response when interacting with large periodic clusters of resonators. These approximations, based on the meso-scale method presented, provide a fast and efficient alternative to addressing large algebraic systems required by meso-scale solutions that naturally appear when the microstructure is dense (see (**6**)). Further, for symmetric flexural structures, the dynamic homogenisation procedure developed here allows us to recover a Rayleigh beam that possesses negative translational and rotational inertia. It has also led to a novel model we term the generalised Rayleigh beam that arrives from the consideration of asymmetric configurations and that retains the dynamic coupling between axial and flexural motions of the main beam.

The approaches presented here are easily extended to modelling the dynamic behaviour of a wide range of multi-structures. They also provide a suitable tool for the design of novel waveguides with generally arranged microstructures that lead to special dynamic responses, which we envisage will also be useful in civil engineering and seismic protection.

Acknowledgements

M.J.N gratefully acknowledges the support of the EU H2020 grant MSCA-RISE-2020-101008140-EffectFact.

References

1. V. Maz'ya and A. Movchan, Asymptotic treatment of perforated domains without homogenization, *Math. Nach.* **283** (2010) 104–125.

2. V. Maz'ya, A. Movchan and M. Nieves, *Green's Kernels and Meso-scale Approximations in Perforated Domains*, Lecture Notes in Mathematics, Vol. 2077 (Springer, Cham, Switzerland 2013).

3. V. G. Maz'ya, S. Nazarov and B. Plemenevskij, *Asymptotic Theory of Elliptic Boundary Value Problems in Singularly Perturbed Domains I, Operator Theory: Advances and Applications*, Vol. 111 (Birkhäuser, Basel 2000).

4. V. G. Maz'ya, S. Nazarov and B. Plemenevskij, *Asymptotic Theory of Elliptic Boundary Value Problems in Singularly Perturbed Domains II, Operator Theory: Advances and Applications*, Vol. 111 (Birkhäuser, Basel 2000).

5. V. Maz'ya, A. Movchan and M. Nieves, Mesoscale asymptotic approximations to solutions of mixed boundary value problems in perforated domains, *Multiscale Model. Simul.* **9** (2011) 424–448.

6. M. J. Nieves, Asymptotic analysis of solutions to transmission problems in solids with many inclusions, *SIAM J. Appl. Math.* **77** (2017) 1417–1443.

7. V. G. Maz'ya, A. B. Movchan and M. J. Nieves, Mesoscale approximations for solutions of the Dirichlet problem in a perforated elastic body, *J. Math. Sci. (N.Y.)* **202** (2014) 215–244.

8. V. G. Maz'ya, A. B. Movchan and M. J. Nieves, Mesoscale models and approximate solutions for solids containing clouds of voids, *Multiscale Model. Simul.* **14** (2016) 138–172.

9. V. G. Maz'ya, A. B. Movchan and M. J. Nieves, Eigenvalue problem in a solid with many inclusions: asymptotic analysis, *Multiscale Model. Simul.* **15** (2017) 1003–1047.

10. A. Bouzerkri and M. Sini, Mesoscale approximation of the electromagnetic fields, *Ann. Henri Poincare* **22** (2021) 1979–2028.

11. V. G. Maz'ya, A. B. Movchan and M. J. Nieves, On meso-scale approximations for vibrations of membranes with lower-dimensional clusters of inertial inclusions, *Algebra i Analiz* (2020) 219–237.

12. A. Cherkaev and M. Ryvkin, Damage propagation in 2d beam lattices: 1. Uncertainty and assumptions, *Arch. Appl. Mech.* **89** (2019) 485–501.

13. A. Cherkaev and M. Ryvkin, Damage propagation in 2d beam lattices: 2. Design of an isotropic fault-tolerant lattice, *Arch. Appl. Mech.* **89** (2019) 503–519.

14. M. Brun, A. B. Movchan and L. I. Slepyan, Transition wave in a supported heavy beam. *J. Mech. Phys. Solids* **61** (2013) 2067–2085.

15. M. Brun, G. F. Giaccu, A. B. Movchan and L. I. Slepyan, Transition wave in the collapse of the San Saba bridge, *Front. Mater.* **1** (2014) 12.

16. M. J. Nieves, G. S. Mishuris and L. I. Slepyan, Transient wave in a transformable periodic flexural structure, *Int. J. Solids Struct.* **112** (2016) 185–208.

17. M. J. Nieves, G. S. Mishuris and L. I. Slepyan, Analysis of dynamic damage propagation in discrete beam structures, *Int. J. Solids Struct.* **97–98** (2016) 699–713.

18. A. Piccolroaz, A. Movchan and L. Cabras, Rotational inertia interface in a dynamic lattice of flexural beams, *Int. J. Solids Struct.* **112** (2017) 43–53.

19. L. Cabras, A. B. Movchan and A. Piccolroaz, Floquet-Bloch waves in periodic networks of the Rayleigh beams: honeycomb systems, dispersion degeneracies and structured interfaces, *Mech. Solids A* **5** (2017) 93–108.

20. G. Bordiga, L. Cabras, D. Bigoni and A. Piccolroaz, Free and forced wave propagation in a Rayleigh-beam grid: flat bands, Dirac cones, and vibration localization vs isotropization, *Int. J. Solids Struct.* **161** (2019) 64–81.
21. K. H. Madine and D. J. Colquitt, Dynamic Green's functions in discrete flexural systems, *Q. J. Mech. Appl. Math.* **74** (2021) 323–350.
22. A. Colombi, D. Colquitt, P. Roux, S. Guenneau and R. V. Craster, A seismic metamaterial: the resonant metawedge, *Sci. Rep.* **6** (2016) 27717.
23. A. Colombi, P. Roux, S. Guenneau, P. Gueguen and R. V. Craster, Forests as a natural seismic metamaterial: Rayleigh wave bandgaps induced by local resonances, *Sci. Rep.* **6** (2016) 19238.
24. S. Won Lee and J. Hwan Oh, Abnormal stop band behavior induced by rotational resonance in flexural metamaterial, *Sci. Rep.* **8** (2018) 14243.
25. M. J. Nieves and M. Brun, Dynamic characterization of a periodic microstructured flexural system with rotational inertia, *Philos. Trans. R. Soc. A* **377** (2019) 20190113.
26. M. Gei, A. B. Movchan and D. Bigoni, Band-gap shift and defect-induced annihilation in prestressed elastic structures, *J. Appl. Phys.* **105** (2009) 063507.
27. A. Banerjee, R. Das and E. Calius, Frequency graded 1D metamaterials: a study on the attenuation bands, *J. Appl. Phys.* **122** (2017) 075101.
28. H. Chen, H. Nasser and G. L. Huang, A study of topological effects in 1D and 2D mechanical lattices, *J. Mech. Phys. Solids* **117** (2018) 22–36.
29. F. Dal Corso, D. Tallarico, N. V Movchan, A. B. Movchan and D. Bigoni, Nested Bloch waves in elastic structures with configurational forces, *Philos. Trans. R. Soc. A* **377** (2019) 20190101.
30. B. Deng, J. R. Raney, K. Bertoldi and V. Tournat, Nonlinear waves in flexible mechanical metamaterials, *J. Appl. Phys.* **130** (2021) 040901.
31. B. Deng, P. Wang, Q. He, V. Tournat and K. Bertoldi, Metamaterials with amplitude gaps for elastic solitons, *Nat. Commun.* **9** (2018) 3410.
32. G. Carta, M. J. Nieves, I. S. Jones, N. V. Movchan and A. B. Movchan, Elastic chiral waveguides with gyro-hinger, Q. J. Mech. Appl. Math. **71** (2018) 157–185
33. M. J. Nieves, G. Carta, I. S. Jones, A. B. Movchan and N. V. Movchan, Vibrations and elastic waves in chiral multi-structures. *J. Mech. Phys. Solids* **121** (2018) 387–408.
34. I. S. Jones, N. V. Movchan and A. B. Movchan, Two-dimensional waves in a chiral elastic chain: dynamic Green's matrices and localised defect modes, *Q. J. Mech. Appl. Math.* **73** (2021) 305–328.
35. G. Carta, M. J. Nieves, I. S. Jones, N. V. Movchan and A. B. Movchan, Flexural vibration systems with gyroscopic spinners, *Philos. Trans. R. Soc. A* **377** (2019) 20190154.
36. M. Iqbal, M. M. Jaya, O. S. Bursi, A. Kumar and R. Ceravolo, Flexural band gaps and response attenuation of periodic piping systems enhanced with localized and distributed resonators, *Sci. Rep.* **10** (2020) 85.
37. Z.-L. Xu, Y.-Q. Wang, R. Zhu and K.-C. Chuang, Torsional bandgap switching in metamaterials with compression-torsion interacted origami resonators, *J. Appl. Phys.* **130** (2021) 045105.
38. Z.-L. Xu, S.-F. Xu and K.-C. Chuang, Coupled flexural-longitudinal waves in an origami metamaterial with uncoupled creases, *Phys. Lett. A* **306** (2021) 127232.
39. D. J. Mead, Wave propagation and natural modes in periodic systems II: multi-coupled systems with and without damping, *J. Sound Vib.* **40** (1975) 19–39.

40. D. J. Mead and Š. Markuš, Coupled flexural-longitudinal wave motion in a periodic beam, *J. Sound Vib.* **90** (1983) 1–24.
41. L. Friis and M. Ohlrich, Coupling of flexural and longitudinal wave motion in a periodic structure with asymmetrically arranged transverse beams. *J. Acoust. Soc. Am.* **118** (2005) 3010. Structure with transverse connection, *Appl. Acoust.* ***72*** (2005) 287–296.
42. L. Friis and M. Ohlrich, Coupled flexural-longitudinal wave motion in a finite periodic structure with asymmetrically arranged transverse beams. *J. Acoust. Soc. Am.* **118** (2005) 3607.
43. Y. Yun and C. M. Mak, A study of coupled flexural-longitudinal wave motion in a periodic dual-beam structure with transverse connection, *J. Acoust. Soc. Am.* **126** (2009) 114.
44. Y. Yun and C. M. Mak, Experimental study of coupled vibration in a finite periodic dual-layered structure with transverse connection, *Appl. Acoust.* **72** (2011), 287–296.
45. G. S. Mishuris, A. B. Movchan and L. I. Slepyan, Waves in elastic bodies with discrete and continuous dynamic microstructure, *Philos. Trans. R. Soc. A* **378** (2020) 20190313.
46. D. V. Evans and R. Porter, Penetration of flexural waves through a periodically constrained thin elastic plate in vacuo and floating on water, *J. Eng. Maths.* **58** (2007) 317–337.
47. Y. Xiao, J. Wen and X. Wen, Flexural wave band gaps in locally resonant thin plates with periodically attached spring-mass resonators, *J. Phys. D: Appl. Phys.* **45** (2012) 195401.
48. S. G. Haslinger, N. V. Movchan, A. B. Movchan, I. S. Jones and R. V. Craster, Controlling flexural waves in semi-infinite platonic crystals with resonator-type scatterers, *Q. J. Mech. Appl. Math.* **70** (2017) 216–247.
49. A. B. Movchan, R. C. McPhedran, G. Carta and R. V. Craster, Platonic localisation: one ring to bind them, *Arch. Appl. Mech.* **89** (2019) 521–533.
50. J. W. Nicholson and L. A. Bergman, Vibration of thick plates carrying concentrated masses, *J. Sound Vib.* **103** (1985) 357–369.
51. P. Wootton, J. Kaplunov and D. Colquitt, An asymptotic hyperbolic-elliptic model for flexural-seismic metasurfaces, Proc. R. Soc. A **475** (2019) 20190079.
52. J.-J. Marigo, K. Pham, A. Maurel and S. Guenneau, Effective model for elastic waves propagating in a substrate supporting a dense array of plates/beams with flexural resonances, *J. Mech. Phys. Solids* **143** (2020) 104029.
53. J.-J. Marigo, K. Pham, A. Maurel and S. Guenneau, Effective model for elastic waves propagating in a substrate supporting a dense array of plates/beams with flexural resonances, *J. Mech. Phys. Solid* **143** (2020), 104029.
54. J. M. Conoir and A. N. Norris, Effective wavenumbers and reflection coefficients for an elastic medium containing random configurations of cylindrical scatterers, *Wave Mot.* **47** (2010) 183–197.
55. A. Gower, I. Abrahams, W. Parnell, (2019): A proof that multiple waves propagate in ensemble-averaged particulate materials, *Proc. R. Soc. A* **475**, 20190344.
56. A. Gower, I. Abrahams and W. Parnell, Multiple waves propagate in random particulate materials, *SIAM J. Appl. Math.* **76** (2019) 2569–2592.
57. A. Gower, R. M. Gower, J. Deakin, W. J. Parnell and I. D. Abrahams, Characterising particulate random media from near-surface backscattering: a machine learning approach to predict particle size and concentration, *Eur. Phys. Lett.* **122** (2018) 54001.
58. K. F. Graff, *Wave Motion in Elastic Solids* (Dover Publications, New York 1975).

Appendix A: Derivation of effective flexural force in the lateral beam

In this section, we derive the effective natural boundary conditions, appearing in (47) and (48), corresponding to equations governing the homogenised medium studied in section 5. Specifically, we refer to the derivation of the effective conditions for the internal shear forces possessed by this medium.

Integral identity for the axial behaviour of the system. We begin by taking (42) and multiplying throughout by a test function $Y \in C^\infty([0, l])$. Next, we apply integration by parts to the result and obtain

$$\begin{aligned}
&\int_0^l \left[Y(x)\mathcal{L}^A_{\text{eff}}\Big(\frac{d}{dx}\Big)U(x) + \omega^2 \Pi_{\text{eff}}(\omega) Y(x) V'(x) \right] dx \\
&\quad = \int_0^l \left[U(x)\mathcal{L}^A_{\text{eff}}\Big(\frac{d}{dx}\Big)Y(x) - \omega^2 \Pi_{\text{eff}}(\omega) Y'(x) V(x) \right] dx \\
&\qquad + \left[Y(x)\sigma\Big(\frac{d}{dx}\Big)U(x) - U(x)\sigma\Big(\frac{d}{dx}\Big)Y(x) \right]_0^l + \left[\omega^2 \Pi_{\text{eff}}(\omega) Y(x) V(x) \right]_0^l, \qquad \text{(A.1)}
\end{aligned}$$

where the differential operator

$$\mathcal{L}^A_{\text{eff}}\Big(\frac{d}{dx}\Big) := EA\frac{d^2}{dx^2} + \omega^2(\rho A + \Psi_{\text{eff}}(\omega)),$$

which embeds effective inertial properties of the medium, and the boundary operator

$$\sigma\Big(\frac{d}{dx}\Big) := EA\frac{d}{dx},$$

is used to represent the internal axial stresses along the rod.

Integral identity for the flexural behaviour of the system. In a similar way, next we multiply (43) by a test function $Z \in C^\infty([0, 1])$, and we apply integration by parts twice to give:

$$\begin{aligned}
&\int_0^l \left[Z(x)\mathcal{L}^F_{\text{eff}}\Big(\frac{d}{dx}\Big)V(x) + \omega^2 \Pi_{\text{eff}}(\omega) Z(x) U'(x) \right] dx \\
&\quad = \int_0^l \left[V(x)\mathcal{L}^F_{\text{eff}}\Big(\frac{d}{dx}\Big)Z(x) - \omega^2 \Pi_{\text{eff}}(\omega) Z'(x) U(x) \right] dx \\
&\qquad - \left[Z(x)\Big\{ Q_{\text{eff}}\Big(\frac{d}{dx}\Big)V(x) - \omega^2 \Pi_{\text{eff}} U(x) \Big\} \right]_0^l + \left[V(x) Q_{\text{eff}}\Big(\frac{d}{dx}\Big)Z(x) \right]_0^l \\
&\qquad + \left[V'(x) M^z\Big(\frac{d}{dx}\Big)Z(x) - Z'(x) M^z\left(\frac{d}{dx}\right) V(x) \right]_0^l. \qquad \text{(A.2)}
\end{aligned}$$

Here, we have introduced a further two differential operators that contribute to characterising the flexural deformation:

$$\mathcal{L}^F_{\text{eff}}\Big(\frac{d}{dx}\Big) := EJ\frac{d^4}{dx^4} + \omega^2 \Upsilon_{\text{eff}}(\omega)\frac{d^2}{dx^2}$$

and

$$Q_{\text{eff}}\Big(\frac{d}{dx}\Big) := -EJ\frac{d^3}{dx^3} - \omega^2\Upsilon(\omega)\frac{d}{dx}.$$

The former contributes to the operator governing the flexural waves in effective medium, whereas the latter contributes to the characterisation of the shear force in the lateral beam, which also embeds the coupling term (see (A.2)). Additionally, we use the operator

$$M^z\Big(\frac{d}{dx}\Big) := EJ\frac{d^2}{dx^2},$$

to describe the internal moments of the medium which take the usual form associated with an ordinary Euler–Bernoulli beam.

Green's identity for the coupled problem. Next, we combine (A.1) and (A.2) and following some rearrangement, we retrieve the integral identity that utilises matrix differential operators:

$$\begin{aligned}
&\int_0^l \Big\{\mathbf{X}(x)\cdot\boldsymbol{L}_+\Big(\frac{d}{dx}\Big)\boldsymbol{W}(x) - \mathbf{W}(x)\cdot\boldsymbol{L}_-\Big(\frac{d}{dx}\Big)\mathbf{X}(x)\Big\}dx\\
&= \Big[\mathbf{X}(x)\cdot\mathbf{F}_+\Big(\frac{d}{dx}\Big)\mathbf{W}(x) - \mathbf{W}(x)\cdot\mathbf{F}_-\Big(\frac{d}{dx}\Big)\mathbf{X}(x)\Big]_0^l\\
&\quad+\Big[V'(x)M^z\Big(\frac{d}{dx}\Big)Z(x) - Z'(x)M^z\Big(\frac{d}{dx}\Big)V(x)\Big]_0^l
\end{aligned} \tag{A.3}$$

where

$$\mathbf{X}(x) = (Y(x), Z(x))^{\mathrm{T}}, \qquad \mathbf{W}(x) = (U(x), V(x))^{\mathrm{T}},$$

$$\mathbf{L}_\pm\Big(\frac{d}{dx}\Big) = \begin{pmatrix} \mathcal{L}^A_{\text{eff}}\Big(\frac{d}{dx}\Big) & \pm\omega^2\Pi_{\text{eff}}\frac{d}{dx} \\ \pm\omega^2\Pi_{\text{eff}}(\omega)\frac{d}{dx} & \mathcal{L}^F_{\text{eff}}\Big(\frac{d}{dx}\Big) \end{pmatrix},$$

and

$$\mathbf{F}_\pm\Big(\frac{d}{dx}\Big) = \begin{pmatrix} \sigma\Big(\frac{d}{dx}\Big) & 0 \\ \pm\omega^2\Pi_{\text{eff}}(\omega) & Q_{\text{eff}}\Big(\frac{d}{dx}\Big) \end{pmatrix}.$$

Finally, the first and second components of the term

$$\mathbf{F}_+\Big(\frac{d}{dx}\Big)\mathbf{W}(x) = \begin{pmatrix} \sigma\Big(\frac{d}{dx}\Big)U(x) \\ Q_{\text{eff}}\Big(\frac{d}{dx}\Big)V(x) + \omega^2\Pi_{\text{eff}}(\omega)U(x) \end{pmatrix},$$

that appears in the right-hand side of (A.3), represents the axial force and the shear force, respectively, possessed by the lateral beam. We note the second component represents the effective shear force in the system and this proves the natural boundary condition arising from integration by parts for the effective beam is that found in (47) and (48).

Appendix B: Derivation of forcing terms required for symmetric flexural systems

Here, we derive the expressions for (69) and (70). In relation to Fig. 11(b), we assume the masses of the flexural resonators located at $y < 0$ have displacement u_j^- and rotation $\theta_j^{(z,-)}$. The governing equations for each of these masses are then

$$-m_j\omega^2 u_j^- = Q_-^{(x,j)}(0) \qquad \text{and} \qquad -I_z^{(j)}\omega^2\theta_j^{(z,-)} = M_-^{(z,j)}(0), \tag{B.1}$$

where $M_-^{(z,j)}$ and $Q_-^{(x,j)}$ are the internal bending moments and shear forces, respectively, in the massless beams forming these resonators. These take the form

$$Q_-^{(x,j)}(\hat{y}) = -E_jJ_j(U_-^{(j)})'''(\hat{y}), \quad \text{and} \quad M_-^{(z,j)}(\hat{y}) = -E_jJ_j(U_-^{(j)})''(\hat{y}),$$

with $U_-^{(j)}$ being the displacement along the massless beams. These displacements have the representation

$$\begin{aligned} U_-^{(j)}(\hat{y}) = &-[(\Theta(a^{(j)}) + \theta_j^{(z,-)})L_j + 2(U(a^{(j)}) - u_j^-)]\frac{\hat{y}^3}{L_j^3} \\ &+[3(U(a^{(j)}) - u_j^-) + L_j(\Theta^z(a^{(j)}) + 2\theta_j^{(z,-)})]\frac{\hat{y}^2}{L_j^2} \\ &-\theta_j^{(z,-)}\hat{y} + u_j^-, \end{aligned} \tag{B.2}$$

with $\hat{y} \in [0, L_j]$. Substitution of (B.2) into (B.1) leads to a system of two equations that can be used to rewrite the generalised coordinates of the masses u_j^- and rotation $\theta_j^{(z,-)}$ in terms of the generalised coordinates $U(a^{(j)})$ and $\Theta^z(a^{(j)})$ describing the motion of the junctions between the lateral beam and the j-th resonator. The results can then be substituted into (B.2) and used to compute:

$$\begin{aligned} \mathcal{Q}_-^{(x,j)} &= Q_-^{(x,j)}(L_j) = -\omega^2\Psi_j(\omega)U(a^{(j)}) + \omega^2\Pi_j(\omega)V'(a^{(j)}), \\ \mathcal{M}_-^{(z,j)} &= M_-^{(z,j)}(L_j) = \omega^2\Pi_j(\omega)U(a^{(j)}) - \omega^2\Upsilon_j(\omega)V'(a^{(j)}). \end{aligned}$$

It remains to use (38) and (39) to obtain (69).

For the axial displacement, we need the function

$$V_-^{(j)}(\hat{y}) = (V(a^{(j)}) - v_j^-)\frac{\hat{y}}{L_j} + v_j^-, \quad 0 < \hat{y} < L_j, \tag{B.3}$$

that describes the axial displacement of the jth resonator located at $y < 0$. Here, v_j^- is the displacement of the mass associated with this resonator in the y-direction. We perform the linear momentum balance in the y-direction for this mass leading to

$$-m_j\omega^2 v_j^- = -F_-^{(y,j)}(0), \tag{B.4}$$

where

$$F_{-}^{(y,j)}(\hat{y}) = E_j A_j (V_{-}^{(j)})'(\hat{y}).$$

Inserting (B.3) into the above and rearranging the result to derive an expression for v_j^-, we then insert this back into (B.3). The axial force supplied by this resonator is then given as

$$\mathcal{F}_{+}^{(y,j)} = \omega^2 \Phi_j(\omega) V(a^{(j)}).$$

Using (38) and (39) then provides (70).